

Journal of Materials Chemistry A

Materials for energy and sustainability

Accepted Manuscript

This article can be cited before page numbers have been issued, to do this please use: Q. Li, J. P. Meng and Z. Li, *J. Mater. Chem. A*, 2022, DOI: 10.1039/D2TA00075J.



This is an Accepted Manuscript, which has been through the Royal Society of Chemistry peer review process and has been accepted for publication.

Accepted Manuscripts are published online shortly after acceptance, before technical editing, formatting and proof reading. Using this free service, authors can make their results available to the community, in citable form, before we publish the edited article. We will replace this Accepted Manuscript with the edited and formatted Advance Article as soon as it is available.

You can find more information about Accepted Manuscripts in the [Information for Authors](#).

Please note that technical editing may introduce minor changes to the text and/or graphics, which may alter content. The journal's standard [Terms & Conditions](#) and the [Ethical guidelines](#) still apply. In no event shall the Royal Society of Chemistry be held responsible for any errors or omissions in this Accepted Manuscript or any consequences arising from the use of any information it contains.

Recent Progress of Schottky Sensors Based on Two-dimensional Transition Metal Dichalcogenides

Qi Li^{a, b, c}, Jianping Meng^{a, d, *}, Zhou Li^{a, b, d, *}

^a CAS Center for Excellence in Nanoscience, Beijing Key Laboratory of Micro–Nano Energy and Sensor, Beijing Institute of Nanoenergy and Nanosystems, Chinese Academy of Sciences, Beijing, 101400, China

^b College of Chemistry and Chemical Engineering, Guangxi University, Nanning, 530004, China

^c Center on Nanoenergy Research, School of Physical Science and Technology, Guangxi University, Nanning, 530004, China

^d School of Nanoscience and Technology, University of Chinese Academy of Sciences, Beijing 100049, China

* Correspondence: mengjianping@binn.cas.cn (Jianping Meng), zli@binn.cas.cn (Zhou Li)

Keywords: Schottky sensors, transition metal dichalcogenides, two-dimensional materials, photodetectors, gas sensors, biosensors, strain sensors

Abstract

2D transition metal dichalcogenides (TMDs), such as MoS₂, MoSe₂, WS₂, WSe₂, etc. have unique physical, chemical, and mechanical properties, and thus they are ideal sensing materials. 2D TMDs-based sensors have proven to be dramatically enhanced in the sensitivity and selectivity by fabricating with Schottky junction, which enables the extensive application in photodetection, gas sensing, biosensing and so on. This review highlights the advances in Schottky sensors that rely on 2D TMDs. The preparation methods of 2D TMDs are described and the selection of proper methods is also discussed. The vital applications of 2D TMDs in Schottky sensors such as photodetectors, gas sensors, strain sensors, and biosensors are summarized and discussed. The structural characteristics and performance parameters of the devices are reviewed. The strategies for fabricating high-performance Schottky sensors are also presented. Finally, an outlook is delivered, and future research directions and challenges are discussed.

1. Introduction

Natural sensing systems bring researchers many ideas for fabricating functional sensors. The sensing technology is able to probe all kinds of physical parameters, such as temperature, pressure, or light intensity, and identify certain chemical species now. The desire to create technologies that enhance the perception of the surrounding environment further drives the progress in the development of physical and chemical sensors. The sensing technology has been advancing for the improving study of materials and fundamental principles.¹

The performances of device are strongly dependent on the materials. Recent years have witnessed a revival of attention to a rather familiar and well-studied class of materials called transition metal dichalcogenides (TMDs), owing to the large surface-to-volume, ratio, facile surface functionalization, mechanical flexibility, etc. The TMDs have been exploited in photonic devices,²⁻⁴ gas sensors,^{5,6} biosensors,^{7,8} strain sensors,^{9,10} electronic devices^{11,12} and energy storage,¹³⁻¹⁶ including the most notable MoTe₂, MoSe₂, MoS₂, WS₂, et al (**Figure 1**).¹⁷⁻²⁰ In 2010, Mak et al.²¹ kindled the first sparks and reported the tunable bandgap in MoS₂ nanosheets depending on the thickness of nanosheets. More surprisingly, they found a transition from an indirect bandgap of 1.3 eV in bulk MoS₂ to a very technologically favorable direct bandgap of 1.9 eV in monolayer MoS₂. A series of subsequent reports makes the start of a new chapter to investigate 2D TMDs. Many 2D TMDs are semiconductors and exhibit great potential to be used in ultra-small and low power transistors that are more efficient than advanced silicon-based transistors and manage ever-shrinking devices.^{22,23} TMDs can be prepared on flexible substrates and survive the stress and strain compliance of flexible supports.²²

2D TMDs are ideal sensing materials and have large exposed surfaces which are available for the interaction of materials and analytes, more active sites to bind analytes selectivity, and good mechanical and processing properties.²⁴ Moreover, the charge transport in 2D materials is strongly confined in the 2D plane, leading to remarkable changes in their electronic properties upon analyte binding.²⁵ Some physicochemical properties are summarized in **Table 1**, such as phase, bandgap, stability, and so on. Typical structural phases for TMDs are 2H and 1T phase, which is shown in **Figure 2a**. 2H phase is the semiconducting phase and is thermodynamically stable for most of the TMDs.²⁶ Inequivalent K and K' points of the Brillouin zone (**Figure 2b**) are the location of valence and conduction bands in single-layer 2H-

phase TMDs that are direct band gap semiconductors. The spin splitting of bands at K is contrary to that at K' owing to time-reversal symmetry.²⁷ Densities of states (DOS), and projected DOS (PDOS) for some TMDs are shown in Figure 2c. Band structures of all pristine 2H-MoS₂ (MoSe₂ and MoTe₂) have direct bandgaps of 1.65 eV (1.40 eV and 1.04 eV) at Γ point. The PDOS of MoS₂(MoSe₂ and MoTe₂) illustrates that Mo states in the conduction and the valence band prevail in PDOS.²⁸ In a word, 2D TMDs have good promise for applications in Schottky-contacted sensors. The Schottky-contacted sensors have good sensitivity and selectivity because the Schottky barrier formed between a semiconductor and metal acts as a 'gate' controller for the current passing through the barrier.²⁹ The current of sensors depends exponentially on the Schottky barrier height, little change in Schottky barrier height leads to the massive change in current, which can enhance the performance of the sensors.^{29,30} It is worthy of extensive study for Schottky-contacted sensors based on 2D TMDs, whatever for gas sensing, photo detecting, biomolecules monitoring or other sensing fields.

Table 1. Typical physicochemical properties for MoTe₂, MoSe₂, WTe₂, WSe₂, MoS₂ and WS₂.

Property	MoS ₂	MoSe ₂	MoTe ₂	WS ₂	WSe ₂	WTe ₂	Ref
Phase	1T, 1H, 3R, 2H (semiconducting phase)						31
Bandgap (eV)	1.8	1.5	1.1	2.1	1.7	0.94	22, 32
Superconductivity (s)	s	s	s	s		s	22
Electron affinity (eV)	3.8	3.5	3.4	3.8	3.5	3.7	33, 34
Environmental stability	Moderate	High	Pretty Low	Fair High	Moderate	Low	35-38
Defection	Vacancies, adatoms, grain boundaries, and substitutional impurities						39, 40
Chemical activity	Reaction with sulphur-containing moieties such as alkanethiol molecules						25

In this critical review, we mainly focus on the current developments of Schottky-contacted sensors based on some kinds of typical 2D transition metal layered nanomaterials, including MoS₂, MoSe₂, WS₂, WSe₂, etc., and other layered materials such as SnS₂, GaSe are compared. The narration stems from the synthesis process for 2D TMDs. Then, the application of Schottky-contacted sensors based on 2D TMDs is summarized in the second part. Moreover, the strategies of performance improvement are also discussed here. Finally, we conclude this

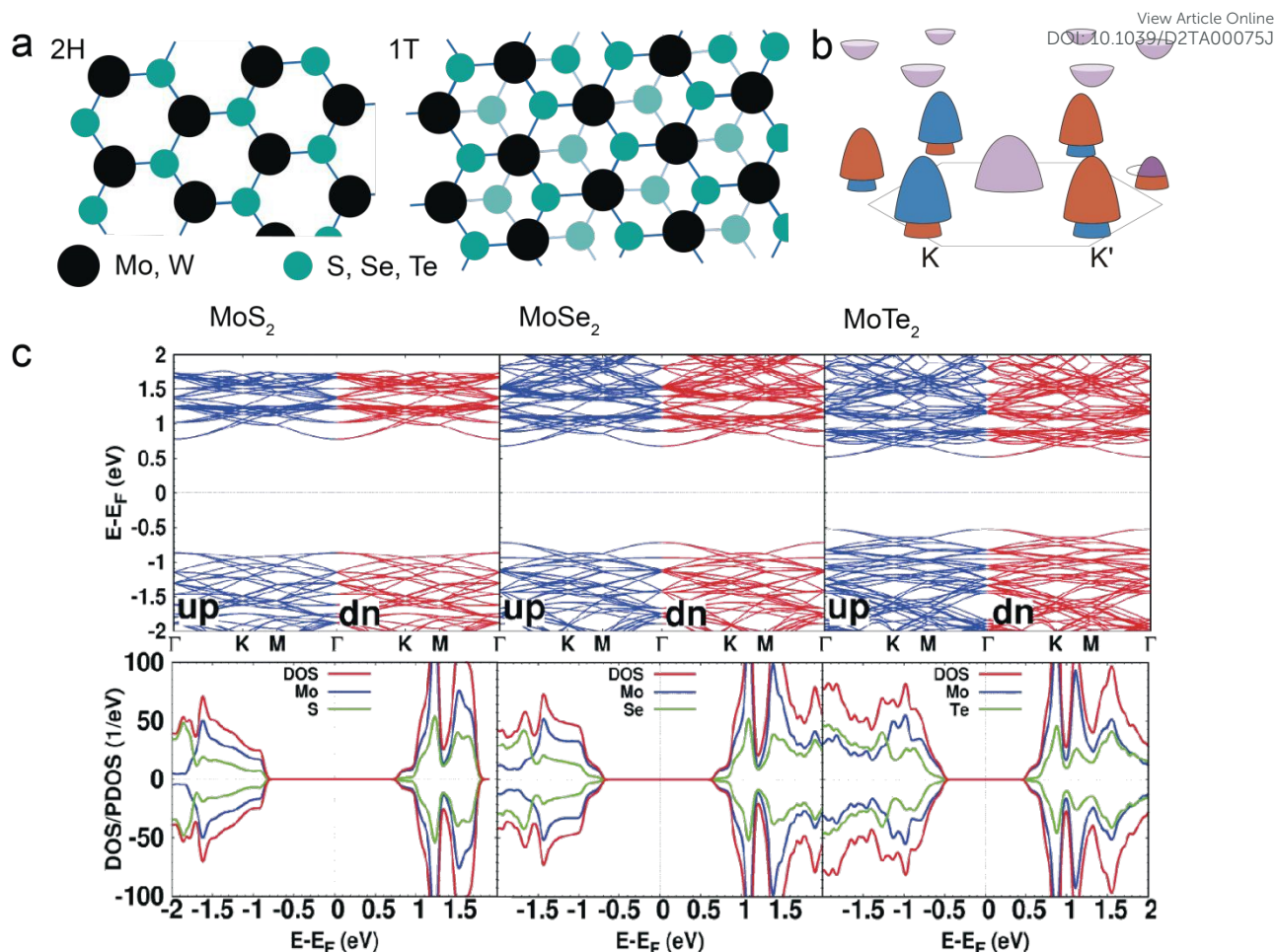


Figure 2. (a) Schematic structures for 2H and 1T phase. (b) Schematic illustration of the electronic band structure of monolayer TMD materials with spin-split valence bands at K and K' points of the Brillouin zone and nearly spin-degenerate valence band at Γ and conduction bands at K and K' points. The spin-up and spin-down bands are red and blue respectively. Reproduced with permission from ref. 27 Copyright 2016 American Physical Society (c) Band structure, and DOS/PDOS for pristine MoS₂, MoSe₂ and MoTe₂. The 'up' and 'dn' in the band structures indicate the spin-up and spin-down components. Reproduced with permission from ref. 28. Copyright 2021 The Royal Society of Chemistry.

article with some perspectives and outlooks on this new trend in sensing field.

2. Synthesis process for 2D TMDs

The structures of 2D TMDs have significant effect on their properties such as size, number of layers, morphologies, orientations, phases, doping, defects, and grain boundaries.⁴¹ Meanwhile, the high quality TMDs with thickness controllability and wafer-scale uniformity are essential for their practical applications of electronics and optoelectronics.²² So, it is of great importance to select suitable approaches that are used for synthesis of 2D TMD materials possessing controlled quality, structure, and other properties.

Generally, there are two ways to prepare 2D TMDs. One is the method of top-down-based exfoliation including mechanical and liquid phase exfoliation; the other is the method of bottom-up-based growth including chemical vapor deposition (CVD), molecular assembly, pulsed laser deposition (PLD), thermal evaporation deposition, and so on. The basic mechanisms for the two methods are illustrated schematically in **Figure 3**. Top-down-based exfoliation involves using bulk crystals to produce single or few-layered TMDs by various physical or chemical driving forces that can break down the Van der Waals interaction in interlayers. By contrast, the bottom-up-based growth is to synthesize the layered materials through precursors such as metal oxide, S powder, et al. Although exfoliation method is mostly used in the fundamental research on physics and devices of TMDs owing to less expensive and good crystalline quality, low production and difficulty of controlling size and shape heavily limit their development beyond the fundamental studies. By comparison, the bottom-up method addresses the issues encountered in top-down methods. For example, the CVD process is able to synthesize single-layer or few-layer 2D TMDs with scalable and reliable large area. However, the CVD method produces TMDs with poor quality as compared to their exfoliated counterparts.

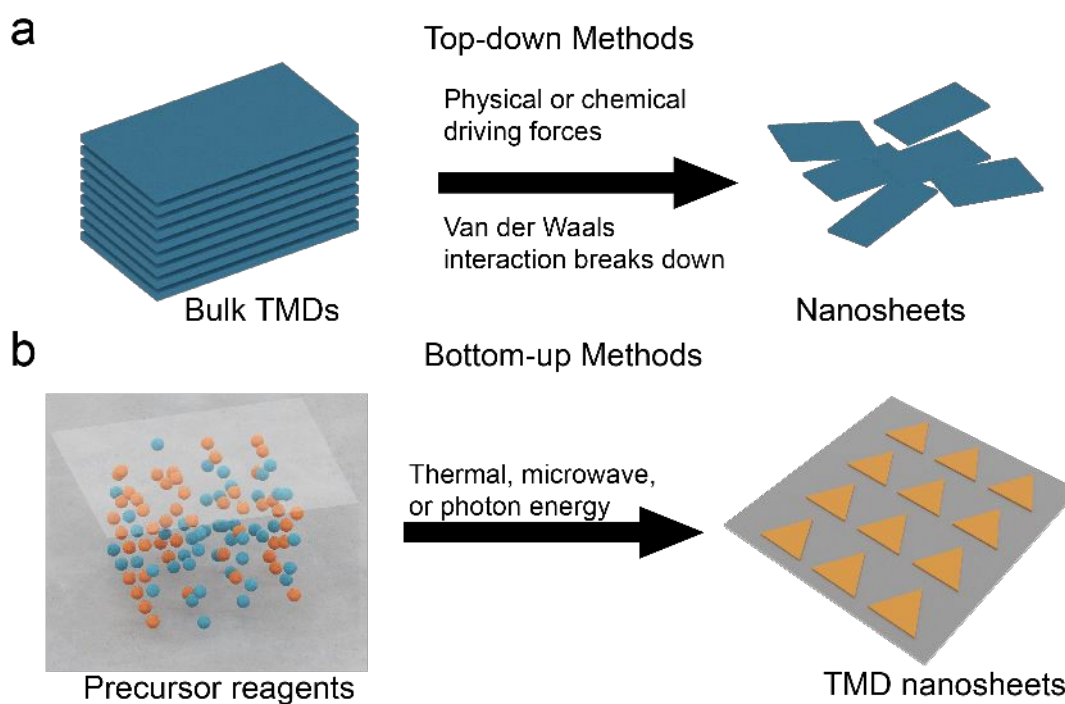


Figure 3. Schematic illustration of mechanisms for (a) top-down methods and (b) bottom-up methods.

2.1. Exfoliation Routes

The exfoliation method can acquire single or few-layer nanosheets from layered bulk crystals directly by using an external source of mechanical, ultrasonic, electrochemical or microwave energy to break the weak van der Waals interaction between the atomic layers. The basic process routes for the methods are shown in **Figure 4a, b**. Figure 4a shows the route for mechanical exfoliation where a tap is used to obtain the layered materials. Figure 4b shows the route for exfoliation in solution where ultrasonic and electrochemical tools are used to obtain layered materials from bulk crystals.

Mechanical cleavage is the first successful and easy method applied to produce single or few-layer nanosheets without expensive and sophisticated equipment. In general, it is a possibility to control the number of atomic layers of 2D TMD nanosheets acquired by mechanical cleavage. Britton et al. used the micromechanical cleavage process to obtain monolayer and bilayer MoS₂ and fabricated corresponding devices with high quality. At low

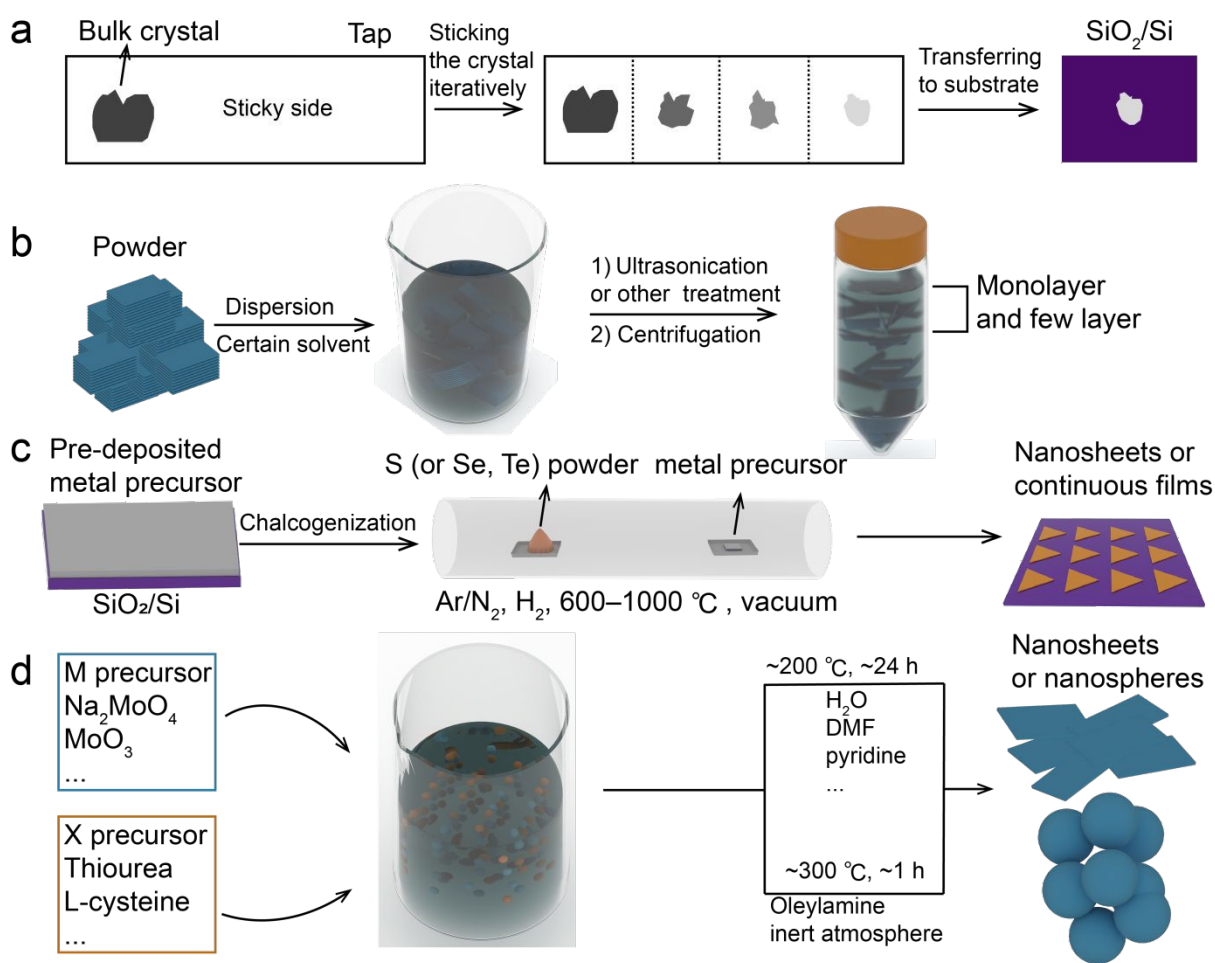


Figure 4. Schematic illustration of the basic routes for (a) and (b) exfoliation methods, (c) vapor deposition methods and (d) solution-based methods.

temperature, both single- and double-layer devices can obtain intrinsic field effect mobilities close to $1000 \text{ cm}^2/(\text{V}\cdot\text{s})$.⁴² The number of layers was hardly controlled by mechanical cleavage, and the atomic processes of the micromechanical cleavage were still poorly understood.⁴³ The nanomechanical cleavage was developed, and the thin flakes of MoS_2 can be exquisitely separated into a single, double to more than 20 atomic layers by an ultra-sharp metal probe.⁴⁴ In order to conquer the limit of mechanical exfoliation in yield, lateral size and contamination, a contamination-free, one-step and universal Au-assisted mechanical exfoliation method is developed (**Figure 5a**).⁴⁵ The products of the method are of millimeter-size and high-quality. Large suspended two-dimensional crystals and heterojunctions are also prepared with high-yield. Such efficient exfoliation is contributed to intensive adhesion between the crystals and the substrates. So far, exfoliation from bulk crystals has not been deemed technologically scalable. Once exfoliation becomes so consistent that the size of the resulting 2D layers is limited only by the dimension and crystallinity of the source crystal, the focus of application-driven materials research may shift toward optimizing the growth of high-quality layered bulk crystals.

Liquid phase exfoliation (LPE) has been used to exfoliate a lot of 2D nanosheets free from defects to produce liquid suspensions by adjusting proper parameters such as graphene and phosphorene. There are two main routes for LPE including sonication and shearing of 2D materials classified by energy source.

Ultrasonic exfoliation is a highly efficient approach to prepare layered 2D TMDs with higher yield than mechanical cleavage. Liquids need to be appropriately chosen (e.g., suitable solvents or surfactants or polymeric solutions), so that the nanosheets will be stabilized against reaggregation. Coleman et al.⁴⁶ investigated a number of solvents used in ultrasonic exfoliation and layered materials including MoS_2 , WS_2 , MoSe_2 , MoTe_2 , TaSe_2 , NbSe_2 , NiTe_2 , BN, and Bi_2Te_3 were efficiently dispersed in solvents. Sonication and exfoliation assisted by nonconventional surfactants, such as DNA/RNA nucleotides,⁴⁷ bovine serum albumin protein⁴⁸ and gelatin⁴⁹ have also attracted much attention. It should be noted that sonication and exfoliation have trouble in controlling nanosheets size. Claudia et al.⁵⁰ exhibited a liquid processing technique exploiting iterative centrifugation cascades, achieving either highly efficient nanosheet size-selection or monolayer enrichment (**Figure 5b**).

Ultrasonic exfoliation of 2D TMDs is simple, low cost and high yield, but powders or high concentration liquid is needed usually from the origin dispersions. Practical application of this method is hindered. So, pure shear force methods for exfoliation for layer materials was developed. The bulk materials can be delaminated into layered forms in organic solvents or surfactant solutions using a high shear laboratory mixer or even a kitchen blender.^{51,52} The mechanism is that exfoliation happens as local turbulent shear rate that is significantly larger than $10^4/s$ can be induced by the rapidly rotating blade. If surface energies of solvents match that of TMD materials, the exfoliation energy is minimized, leading to shear exfoliation at low shear rates. This method can achieve controlling the nanosheets length between ~ 40 and ~ 200 nm and the thickness between ~ 2 and ~ 12 layers.⁵² Liquid shear exfoliation technique has been improved for mass production of MoS₂ nanosheets with high yield and good quality. The feasible strategy is to use a green mixed solvent system of ethanol/water to generate MoS₂ nanosheets.⁵³ The best ratio and initial concentration for optimal shear exfoliation are 45 vol% and 10 mg/mL, respectively. Besides, when the number of shear cycles reaches 10, the theoretical yield can attain nearly 30%, and the residue and solute can also be recycled for the next shearing exfoliation without introducing any new impurities.

Chemical exfoliation is a method to intercalate various guest species, including simple atomic species, alkali metals, polymers, and organometallic species into the van der Waals gap between the neighboring layers of 2D TMDs and produce nanosheets such as MoS₂, WS₂, ZrS₂.^{54,55} Among different intercalants, large organolithium compounds (n-butyllithium (n-BuLi) and tert-butyllithium (t-BuLi)) are significantly efficient intercalants in the chemical exfoliation approach.⁵⁶ Although it is a facile and effective approach to produce layered TMDs through intercalation of organolithium salts and exfoliation, there are some drawbacks for this method, such as nanosheets are sub-micron lateral sizes, low yield of monolayer TMDs, being subjected to ambient atmosphere, and semiconducting properties disappearing. Alternative guest species have been drawn much attention and exploited to produce large sized monolayer nanosheets with high yield in recent years. For example, Lin et al.⁵⁷ acquired highly uniform, phase-pure semiconducting nanosheets, using the electrochemical intercalation of quaternary ammonium molecules (such as tetraheptylammonium bromide) into 2D crystals, followed by a mild sonication and exfoliation process.

2.2. Vapor Deposition

View Article Online
DOI: 10.1039/D2TA00075J

Different from exfoliation routes, direct growth by vapor phase deposition, especially chemical vapor deposition, enables the scalable and controllable preparation of 2D TMDs with high quality and large area, which is of great significance for research of 2D TMDs. The basic routes are shown in Figure 4c. Firstly, pre-deposited metal precursors are obtained and then the chalcogenization of the precursors is conducted in a certain reaction atmosphere to obtain nanosheets or continuous films.

Chemical vapor deposition (CVD) is a universal and less expensive technique compatible with industry. Large-area monolayer and few-layer TMD films can be synthesized by this method. Moreover, CVD meets the requirements for the development of practical devices as producing high-quality TMD nanosheets with scalable lateral sizes and controllable thicknesses. Size, morphology, phase, and any interfaces present of 2D materials can be controlled by rational design and careful tuning of the growth processes. Hence, it is important to explore how parameters such as the precursor, substrate, pressure, and temperature affect mass and heat transport, and interface reactions during CVD growth of 2D TMDs. Solid sources are generally used for synthesis of TMDs. Metal (molybdenum or tungsten) sources are often transition metal oxides (e.g., MoO_3 , WO_3) or chlorides (MoCl_5) or metal foils. Meanwhile, the sources of sulfur or selenium were from S or Se powders.⁵⁸ Vapor pressure of solid sources is influenced by temperature seriously, thus it is essential to control temperature in source zone accurately. High quality TMDs can generally be acquired at considerably high temperatures besides at the price of high energy consumption and limited suitable substrates.⁵⁸ Moreover, it is significant to control number of layers of 2D TMDs through modulating temperature.⁵⁹ Substrates have great effects on the growth of 2D materials due to their various microstructures and lattice structures. Generally, substrates such as inert Si/SiO₂, mica and polyimide are used to grow 2D TMDs.⁶⁰⁻⁶² Sapphire substrates are different from some other substrates. C-plane sapphires have specific lattice orientation and the atomically smooth surface.^{63,64} The pressure of chamber ranged from a few atmospheres to several millitorr or even lower, which leads to enormous effect on the gas flow behavior in a CVD chamber. Thus, it uses a low-pressure CVD approach to grow wafer-scale, continuous 2D TMD films.⁶⁵

Morphology control is also important to understand the relationships between the structure and performance of 2D materials in catalysis, sensors, and energy applications.

In recent years, 2D MoS₂, WS₂, WSe₂ and MoTe₂ with large areas and single crystals have been prepared using CVD method.⁶⁶⁻⁷⁰ 2D TMDs with a large area and a single crystal have an overriding importance to their application. On the one hand, electronic, mechanical and thermal properties of 2D TMDs may be suppressed by grain boundaries.⁷¹ On the other hand, it is prior to take advantage of large area 2D materials to fabricate devices based on current silicon-based semiconductor technology. Dumitru et al. employed epitaxial CVD to synthesize monolayer MoS₂ with controllable lattice orientation on the atomically smooth surface of the sapphire as a substrate.⁷² The shapes of these single-crystal MoS₂ are well-defined equilateral triangles merged into a continuous monolayer film with an area of 6 mm × 1 cm in the middle of the substrate (Figure 5c).

Properties of 2D TMDs can be tunable by controlling the number of layers. For example, indirect band gaps of multilayer TMDs such as MoS₂, MoSe₂ and WS₂ change to direct band gaps of monolayer TMDs, which accounts for potential applications in light-emitting diodes (LEDs), laser diodes, and photovoltaic (PV) devices. It provides versatility to stack up 2D TMDs layer by layer and fabricate multifunctional van der Waals heterostructures for new properties and novel devices.⁷³ Number of layers in TMDs can be adjusted by changing the reaction conditions in CVD reaction. For example, monolayer, bilayer, and three to four layers MoSe₂ form when temperatures are 750, 825 and 900°C respectively in the CVD process.⁵⁹ Although the size, number of layers, morphologies, orientations, and phases can be regulated by changing the parameters of the synthesized process. Intrinsic properties of specific 2D materials were limited, while elemental doping is an excellent protocol to tune the properties of 2D TMDs. Monolayer W_xMo_{1-x}S₂ (≈20 μm in size) in a triangle shape was successfully grown by CVD under one atmospheric pressure.⁷⁴ Wafer-scale, continuous films of 2D materials are urgently needed for applications in electronic and optoelectronics as they are compatible with the current silicon-based microfabrication processes. In order to obtain high quality continuous films, there are even some modified CVD methods such as MOCVD (metal-organic CVD), LPCVD (low-pressure CVD), and ICP-CVD (inductively coupled plasma CVD).⁷⁵⁻⁷⁸ Recently, a breakthrough that the 4-in. wafer-scale, homogeneous MoS₂ and WS₂

films were grown by using gas-phase $\text{Mo}(\text{CO})_6$, $\text{W}(\text{CO})_6$, and $(\text{C}_2\text{H}_5)_2\text{S}$ as precursors, and H_2/Ar as carrier gas was made.⁷⁹

CVD is also one of the most appropriate choices to produce 2D heterostructures, especially lateral 2D heterostructures that need strict requirements.⁸⁰⁻⁸⁴ There are several kinds of heterostructures including metal/semiconductor junctions, semiconductor/semiconductor junctions, semiconductor/insulator junctions, metal/insulator junctions.

Atomic layer deposition (ALD) is significant to grow atomically thin films with the controllable manner. ALD is one of the primary thin film deposition techniques and may be applied in industrial production of 2D TMDs. Using ALD to synthesize TMD films can date back to 2004, when the solid lubricant thin films of the crystalline WS_2 were grown by atomic

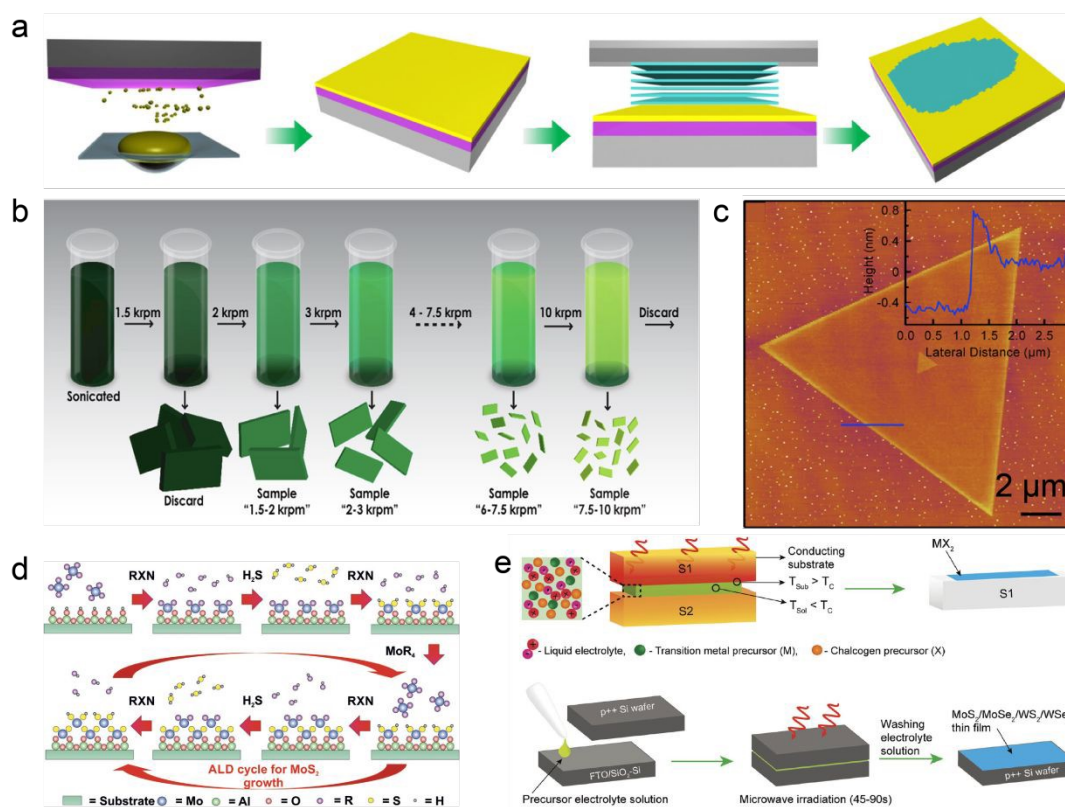


Figure 5. (a) Schematic of the exfoliation process. Reproduced with permission from ref. 45. Copyright 2020 Springer Nature (b) Schematic describing the basic centrifugation cascade. Reproduced with permission from ref. 50. Copyright 2016 American Chemical Society. (c) Atomic force microscope image of a monolayer MoS_2 grain. Inset: Line scan showing the thickness profile along the blue line in the AFM image. Schematic describing the basic centrifugation cascade. Reproduced with permission from ref. 72. Copyright 2015 American Chemical Society. (d) Proposed scenario for MoS_2 film growth by ALD using $\text{Mo}(\text{NMe}_2)_4$ and H_2S in an A–B cycle; RXN: reaction. Reproduced with permission from ref. 87. Copyright 2017 Wiley. (e) Schematic of the WSe_2 thin film synthesis directly on a p^{++} Si wafer. Reproduced with permission from ref. 95. Copyright 2017 Wiley.

layer deposition (ALD) using WF_6 and H_2S as gas precursors.⁸⁵ However, preparing ultrathin TMDs through ALD emerged in 2014.⁸⁶ So far, various monolayer and few layer TMD films have been synthesized with large area uniformly and reproducibly, including MoS_2 , WS_2 and WSe_2 .³¹ Low-temperature synthesis of MoS_2 films is achieved by using volatile $\text{Mo}(\text{NMe}_2)_4$ and H_2S as precursors at low temperature of 60 °C in an ALD system (Figure 5d). Number of layers can be controlled precisely as the growth rate of MoS_2 was 0.12 nm/cycle.⁸⁷

Conventional high temperature growth of 2D TMD materials is not suitable for flexible substrates used for flexible electronic and optoelectronic devices, wearable sensors, and other portable devices. So, there are some solutions to these obstacles. Recently, Phan et al. designed a direct one-step method to transfer MoS_2 films on sapphire or SiO_2/Si substrates to a PET substrate by a mediator of epoxy glue and a lack of etching process.⁸⁸

Pulsed laser deposition (PLD) has also been utilized to grow TMD nanosheets that have good crystallinity comparable to that grown by CVD.^{89,90} A scalable PLD method was developed to deposit wafer-scale MoS_2 on various substrates, such as SiO_2 , HfO_2 , sapphire and quartz achieving control over the thickness (1–10 layers) precisely and in situ by regulating target and parameters of PLD. Sulfur vacancies in the MoS_2 films may decrease by using the target with excess sulfur element.⁹¹ It is reported that the higher laser energy density and temperature contributed to high crystalline orientation of the film, and stoichiometry and purity of the films can be changed by adjusting pressure and environment of the deposition chamber.⁹²

2.3. Solution-based synthesis

Wet chemical synthesis involves chemical reactions that are used to produce a variety of nanomaterials with a high yield under the condition of high temperature and high pressure. The basic routes of solution-based synthesis are shown in Figure 4d. This method uses M precursors and X precursors (MX_2 represents TMDs) to synthesize in the solution under 200 to 300 °C and to obtain nanosheets, nanospheres or other morphology. There are three categories of the method containing hydrothermal, solvothermal and colloidal routes. It is useful for hydro/solvothermal to synthesize a kind of morphologies and nanostructures. The islands of 1T- MoS_2 within few-layer nanosheets of 2H- MoS_2 (1T@2H- MoS_2) are prepared via the solvothermal treatment in ethanol.⁹³ The 1T@2H- MoS_2 nanosheets show better electrical

conductivity and exhibit ferromagnetism. Applying colloidal chemistry in synthesis of large-scale MoS₂ nanosheets, the MoS₂ nanosheets obtained from this method display excellent uniformity of size and thickness distributions, the same as exfoliated MoS₂.⁹⁴ Well-dispersed nanosheets can be used in spray-coating to fabricate a uniform film over a 4-in. wafer. A method of one-step quick synthesis (within 45–90 s) is developed to prepare TMD films (MoS₂, WS₂, MoSe₂, WSe₂, etc.) with microwave irradiation on solid substrates (Figure 5e).⁹⁵ The number of the quintuple layers of the TMD thin films can be precisely controlled by using different concentration of the precursor in the electrolyte solution.

Thermal decomposition is the route that involves decomposition of a single-source precursor in an inert or reducing atmosphere at elevated temperatures. The polycrystalline MoS₂ and WS₂ layers are synthesized by thermolysis of a (NH₄)₂MoS₄ and (NH₄)₂WS₄ precursor solution followed by a two-step annealing process.⁹⁶ It is a significant advancement to synthesize high-quality MoS₂ on a plastic substrate directly at the temperature, which is beneficial to flexible optoelectronic applications.⁹⁷

The features of commonly used preparation methods are shown in **Table 2**. Mechanical cleavage yields nanosheets with the highest quality. Nanosheets obtained by vapor deposition and liquid phase exfoliation have medium crystalline quality. Using solution-based methods will make nanosheets have poor crystalline quality, some structural defects and crystal

Table 2. Advantages and disadvantages for four commonly used preparation methods.

Production method	Advantages	Disadvantages
Mechanical cleavage	Highest crystalline quality, simple and low-cost	Lowest yield, finding samples is usually time consuming
Vapor deposition	Thickness and lateral dimension can be modulated. Industrially scalable	Fair crystalline quality
Liquid phase exfoliation	Highest yield, stable dispersion of nanosheets in solution	Time and energy consumption, rare monolayer
Solution-based methods	Nanoparticles, even quantum dots, can be obtained. Industrially scalable	Structural defects and crystal distortions; the larger the nanosheets produced, the thicker they are.

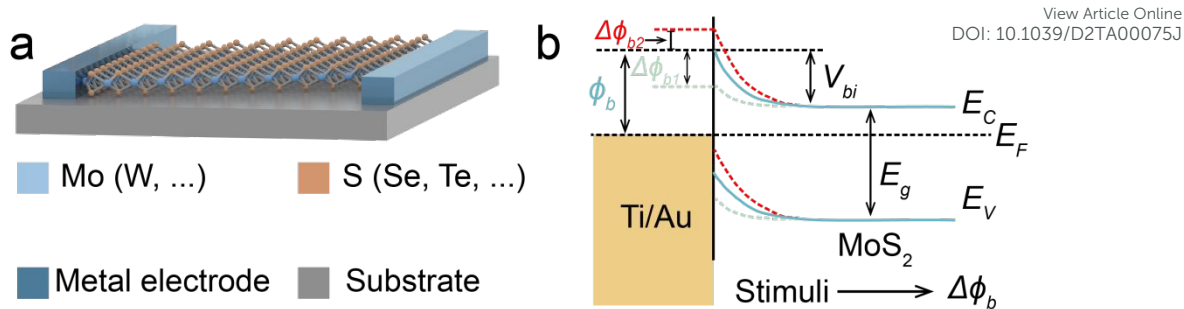


Figure 6. (a) The typical configuration of TMD-based Schottky sensors. (b) The sensing mechanisms for Schottky sensors.

distortions. Liquid phase exfoliation has the highest yield and vapor deposition the second highest. Mechanical cleavage has the lowest yields and makes finding samples usually time consuming. Both thickness and lateral dimension can be modulated by the vapor deposition method, respectively. However, for liquid phase exfoliation, the larger the nanosheets produced, the thicker they are. Nanoparticles, even quantum dots, can be obtained by liquid phase exfoliation and solution-based synthesis.

3. Application of Schottky sensor based on the 2D TMDs

Schottky sensor based on the 2D TMDs are fabricated by forming Schottky heterojunction between TMDs and metal or metal-like materials. The interaction between Schottky sensors and ambient species will affect the Schottky barrier height. The current of the sensor is highly correlated with Schottky barrier height, so a slight change in Schottky barrier height will also result in a strong change in current. Sensitivity and selectivity of sensors can be improved strongly by the Schottky contact. The typical configuration of Schottky-contacted sensors and their sensing mechanisms are summarized in **Figure 6**. In recent years, 2D TMDs-based Schottky sensors have received much attention for applications in photodetection, gas sensing, biosensing and so on.

3.1. Schottky-contacted photodetectors

Photodetection capability of a photodetector was affected by the device configuration. Photodetectors with ohmic contact generally have advantages in great photoconductive gain and high responsivity. Compared to photodetectors of ohmic junction, the Schottky-junction photodetectors are of great sensitivity and quick response speeds. More importantly, Schottky-junction photodetectors are capable of detecting light illumination without an external bias

voltage, because the built-in potential achieves the separation and transport of the photogenerated carriers.

A conventional photodetector with a metal-semiconductor-metal structure is significantly affected by Schottky contact formed between the semiconductor and metal. So, great efforts have been devoted in studying the effect of Schottky contact with different metals on devices. Zhang et al.⁹⁸ fabricated monolayer WSe₂ phototransistors using CVD method and conducted the specific investigation of effect of the Schottky contact on optoelectronic properties of the devices. The p-type transistors using high work function Pd metal contact have a low Schottky barrier height. ON/OFF current ratio reaches 10⁹ and mobility is larger than 7.3 cm²/(V·s). The external photo gain of the Pd-contacted device is 3.5×10⁵ and the specific detectivity is more than 10¹⁴ Jones. However, the photocurrent for the Pd-contacted devices spends more than 5 s reaching a plateau in ambient atmosphere. In contrast, WSe₂ devices using low work function metal-Ti have a high Schottky barrier, displaying much faster response time less than 23 ms and better photocurrent linearity as a function of incident optical power. Because the photogenerated electron–hole pairs can be separated effectively for the high voltage drop within long depletion region. Besides the p-type WSe₂, n-type MoS₂ is often used the materials of Schottky-junction photodetector. A Schottky-junction photodetector based on the monolayer MoS₂ and Pd electrodes is fabricated.⁹⁹ The photosensitivity is greatly improved compared to multilayer MoS₂. Direct bandgap of monolayer MoS₂ is beneficial for photo-induced carrier generation. The device presents the great response speed advantage over photoconductive detectors with ohmic contact which takes several seconds for current decay. Son et al.¹⁰⁰ demonstrated the switchable photoresponse of monolayer WSe₂–MoS₂ lateral heterostructure by photoconductive spectral atomic force microscope (**Figure 7a**). The authors found that a PtIr coated tip was brought into contact with a thin WSe₂ or MoS₂ crystal, and a Schottky barrier formed at the interface for the difference between the work function of metal and the valence (conduction) band edge of WSe₂ (MoS₂). Two single-layered component crystals display greatly different electrical properties which reveals a critical role of junction barrier in the carrier transport behavior through the nanoscale metal-atomically thin 2D crystal interface. Some intrinsic properties of the TMDCs channel are masked by the Schottky contacts resulting from the metal–semiconductor interface. However, devices based on such 2D–2D van

View Article Online
DOI: 10.1039/C2JA00075J

der Waals heterostructures (vdWHs) are subject to the great interlayer coupling and finite adjustment of the electronic structure for the two vested 2D TMDs, which results in poor performance of the devices. Specifically, the overall optical absorption and spectral selectivity are blocked by atomically thin property and availability of the two layered TMDs, which is crucial to photocarrier generation efficacy. Thus, Wu et al.¹⁰¹ came up with a strategy to tack the problems (Figure 7b). All-inorganic cesium lead halides perovskite CsPbI_{3-x}Br_x QDs (PQDs) is integrated with monolayer MoS₂ to fabricate a photodetector. Due to the synergistic effect of photogating effect and the modulation of the Schottky barriers, the photodetector exhibits the high photoresponsivity of 7.7×10^4 A/W, detectivity of 5.6×10^{11} Jones, and an ultrahigh external quantum efficiency exceeding 107% under 1.5 μ W illumination of 532 nm ($V_D=1$ V). Modulation of architecture should be another way to address the above issue. A vertical Schottky-contact photodetector by interlaying the multilayer WSe₂ between an Au electrode and an ITO electrode is fabricated (Figure 7c).¹⁰² The devices show high responsivity of 1 A/W (0.5V) and fast response time of 50 μ s under 0.567 mW/mm² illumination of 637 nm. Moreover, the photodetector displays broadband photoresponse from 550 nm to 950 nm. Their results demonstrate that the vertical Schottky-contacted devices based on 2D TMDs can obtain excellent photoelectric response. The ultrashort vertical channel length as well as the built-in electric-field accounts for the fast response. In terms of photodetectors, Schottky-junction photodetectors with the asymmetric structure at both ends demonstrate the high performance because the carriers generated by photoexcitation are separated by built-in potential at the high Schottky barrier height and, the separated electrons and holes only need to pass through the lower Schottky barrier easily before being collected. Wu et al.¹⁰³ fabricated MoS₂ field-effect transistor (FET) and investigated different charge carrier transport properties in the metal–semiconductor interfaces of asymmetric metal contacts (Au–Cr) (Figure 7d). Au and Cr electrodes act as drain and source electrodes to form ohmic and Schottky contact with MoS₂, respectively. The devices exhibit electrical rectifying characteristic whose current rectifying ratio is more than 10³ and have an ideal factor of 1.5. The devices also exhibit different sensitivities to the light (green light emitting diode with the center wavelength at about 519 nm) under external bias in the opposite directions, with the highest photoresponsivity reaching 1.1×10^4 A/W and specific detectivity up to 8.3×10^{12} Jones at a forward drain bias

of 10 V. Although the modulation of device structure is an effective way to improve the performance of a photodetector, the modification of materials is an intrinsic way to enhance the performance of a photodetector. Recently, some metal dichalcogenides such as SnS₂, InSe₂, and SnSe₂ have the similar structure to TMDs and can be used for photodetection. Sb-doped SnS₂ monolayers can improve metal-semiconductor interface (Figure 7e).¹⁰⁴ The device demonstrates that the high mobility of the transistors with n-type behavior based on the Sb-doped SnS₂ monolayers is one order of magnitude higher than that of pristine SnS₂ transistors. The photoresponsivity (R) and external quantum efficiency (EQE) of Sb-SnS₂ monolayers phototransistors approached three orders of magnitude higher than those of the pristine SnS₂ phototransistors. Sb-doped SnS₂ has improved metal–semiconductor interface by decreasing of Schottky barrier width. Moreover, doping plasmonic metal nanoparticles can also enhance the optical absorbance owing to the localized surface plasmonic resonance (LSPR) effect. However, doping can introduce some defects, leading to suppression of the device performance. With that in mind, a photodetector based on non-contact plasmonic Ag NPs and few-layer SnSe₂ is designed to demonstrate the significant enhancement of performance.¹⁰⁵ As a result, responsivity of SnSe₂/AgNP:SiO₂ photodetector is enhanced by 881, 430, 40 and 11 times compared with the devices without Ag NPs under illumination of 405, 635, 1310, and 2200 nm light. Furthermore, the lattice structure of SnSe₂ is perfectly preserved.

In the case of conventional Schottky-junction photodetectors, a bias is essential to enhance the separation of electrons and holes, which leads to the highly power consuming. A kind of self-powered photodetectors are designed and cause extensive research nowadays. According to the construction mechanism, self-powered photodetectors are based on the photovoltaic effect in the built-in potential of Schottky junction.¹⁰⁶ Consequently, Zhou et al.¹⁰⁷ constructed a MSM (metal–semiconductor–metal) photodetector based on WSe₂ flakes where different contact lengths were chosen for the two metal–semiconductor contacts forming asymmetric geometry. The self-powered photodetector exhibits a large photocurrent under zero bias and a small dark current. The responsivity of 2.31 A/W is obtained under zero bias. This MSM photodetector can overcome the disadvantage of high dark current in traditional MSM photodetectors. The dark current of ≈ 1 fA as well as detectivity of 9.16×10^{11} Jones is obtained under illumination of 650 nm with the power of 27 pW. However, the small photocurrent of

the self-powered photodetector with Schottky junction hinders their practical applications. Surface plasmon enhancement of photodetector by quadrupole is utilized to overcome the disadvantage of an asymmetric Schottky-junction photodetector which is constructed with InSe/Au and a dual-band property.¹⁰⁸ The self-powered InSe/Au device exhibits responsivity of 369 mA/W under 365 nm illumination with a high on-off ratio up to 10^3 . Compared to original InSe photodetectors, InSe/Au photodetectors realize photodetection in UV-vis-NIR broadband region. The photodetection band in the long wavelength region

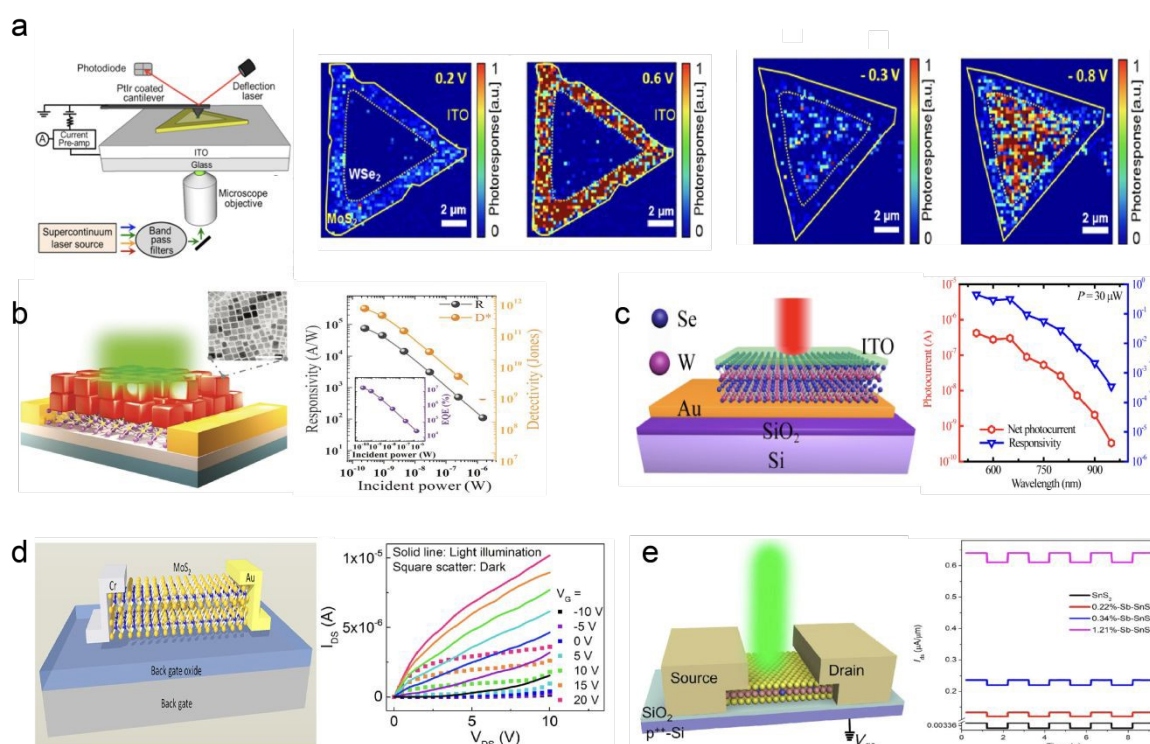


Figure 7. (a) Schematic illustration of the photoconductive spectral atomic force microscope (PCS-AFM) instrument and WSe_2 - MoS_2 heterostructure crystal and current maps generated by conductive AFM measurements in the dark under applied sample bias voltages. Reproduced with permission from ref. 100. Copyright 2016 American Chemical Society. (b) Schematic model of the device with its inset shows a typical TEM image of the PQDs (The scale bar is 50 nm) and responsivity and specific detectivity with an inset shows the EQE as a function of illumination power of the phototransistor. Reproduced with permission from ref. 101. Copyright 2018 Wiley. (c) Schematic of Au- WSe_2 -ITO devices and responsivity and net photocurrent versus wavelength. Reproduced with permission from ref. 102. Copyright 2018 IOP (d) Schematic 3D view of the transistor based on MoS_2 channel with asymmetric electrodes (Au-Cr) and the linear output curves of the device with Au-Cr electrode in dark and under light illumination at forward V_{DS} . Reproduced with permission from ref. 103. Copyright 2018 American Chemical Society. (e) Schematic of the Sb-doped SnS_2 monolayer photodetector and corresponding time dependent I_{DS} of the SnS_2 and Sb-doped SnS_2 monolayers phototransistors with the laser switching on and off under a positive $V_{DS} = 1$ V. Reproduced with permission from ref. 104. Copyright 2019 Springer.

roots in a high wavelength selective enhancement of pristine responsivity. The enhanced ratio of responsivity reaches a peak value of $\sim 1200\%$ at the wavelength of 685 nm. Detectivity of 3.35×10^{12} Jones was obtained at 685 nm. A high-performance visible to near-infrared (470–980 nm) photodetectors can be also realized by using AuCl₃ doped InSe.¹⁰⁹ This photodetector can operate without gate bias. Responsivity (R) and detectivity (D*) are 19300 A/W and $\approx 3 \times 10^{13}$ Jones for 470 nm light. R and D are 7870 A/W and $\approx 1.5 \times 10^{13}$ Jones for 980 nm light.

However, metal layer in Schottky junction photodetector absorbs light heavily, which will limit the photoelectric conversion efficiency of the photodetector severely. Consequently, it was reported that the use of transparent indium tin oxide (ITO) glass as an electrode can avoid that weakness of the photodetector. A photodetector with a vertical Schottky structure based on Au–MoS₂–ITO is constructed using the transparent ITO glass as the electrode.¹¹⁰ The response time of ≈ 64 μ s, a stable photoresponsivity of ≈ 1 A/W, photocurrent to dark current ratio of 10^6 , and a dark current of 10^{-12} A are obtained at a zero bias under 3.38 mW/mm² ($\lambda = 637$ nm) illumination. Subsequently, a similar-structure photodetector is fabricated based on WSe₂,¹¹¹ which has a broadband photoresponse of 550–950 nm and photoresponsivity of ≈ 0.1 A/W.

3.2. Schottky-contacted gas sensors

Recently, gas sensors with Schottky junction have been demonstrated to possess excellent performances with the high sensitivity, selectivity, and low working temperature. Some of these sensors based on 2D TMDs are fabricated by creating a heterojunction between a 2D TMD and metal or metal-like materials. 2D TMDs are applied in gas detection extensively for their excellent physicochemical and electrical properties.¹¹²

Most of the gas sensors consisting of Schottky junction between 2D TMDs and other materials can be regarded as a kind of chemiresistive or chemical field-effect transistors (chem-FETs), which operate according to the charge transfer process upon interaction with gas molecules or vapors by withdrawing electrons or accepting electrons. A high-performance gas sensor based on Schottky junction between monolayer MoS₂ and Ti/Au, which can work at room temperature, is developed (**Figure 8a**).¹¹³ The Schottky barrier can be modulated by exposing the devices to NO₂ and NH₃ gases. Specifically, the Schottky sensors exhibit the

sensitive detection of NO_2 and NH_3 down to 20 ppb and 1 ppm, respectively. The reason for this sensing behavior should be explained by charge transfer between gaseous species and MoS_2 monolayers, and the modulation of Schottky barrier at the MoS_2 -metal electrode junctions. Obviously, the modulation of the Schottky barrier greatly accounts for significant improvement of sensitivity.

Layered MoTe_2 is also an ideal candidate for sensitive gas sensors. A back-to-back Schottky diode based on few-layer MoTe_2 is fabricated to detect NO_2 and NH_3 (Figure 8b).¹¹⁴ The ON/OFF current ratio of the α - MoTe_2 (α phase) devices reach 10^3 and the operation voltage is 5 V. The authors experimentally assess the performance of the Schottky diode devices and FET

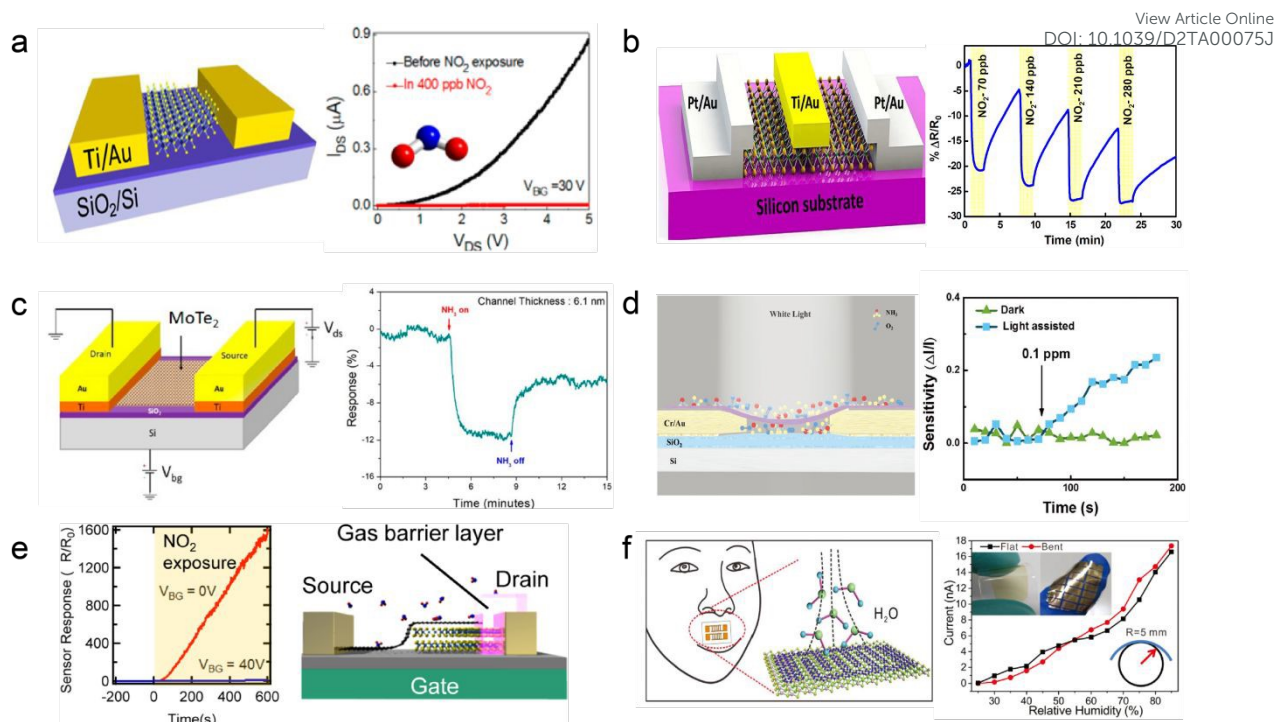


Figure 8. (a) Schematic of the back-gate MoS₂ FET and conductance change of MoS₂ FETs upon exposure to 400 ppb of NO₂. Reproduced with permission from ref. 113. Copyright 2014 American Chemical Society. (b) Schematic of a MoS₂ FET with ionophore and output signal of MoS₂ devices indicating that the sensors are able to detect AsO₃²⁻ down to 0.1 ppb. Reproduced with permission from ref. 114. Copyright 2018 The Royal Society of Chemistry. (c) Schematic of back-gate FET connection and Response to 100 ppm NH₃ in air of 6.1 nm thick MoTe₂ devices. Reproduced with permission from ref. 115. Copyright 2019 MDPI. (d) The side view of the testing device with suspended SnS₂ layers and the real-time response of the suspended sensor under dark and white light assistance when exposing to 0.1 ppm concentration. Reproduced with permission from ref. 116. Copyright 2018 Wiley. (e) Time-dependent sensor responses of GMH under different gate voltages ($V_{BG} = 0$ and 40 V) in linear scale and schematic of the GMH device with a gas barrier layer. Reproduced with permission from ref. 120. Copyright 2018 American Chemical Society. (f) The cartoon shows the sensor used to monitor human breath and current response of the flexible sensor working in flat and bent states, respectively. Reproduced with permission from ref. 124. Copyright 2017 The Royal Society of Chemistry.

devices for gas sensing with exposure to different concentrations of NO₂ and NH₃. It is rather remarkable that the α -MoTe₂ Schottky diode shows a faster response and recovery time for NH₃ and NO₂ than the α -MoTe₂ FET owing to Schottky barrier of MoTe₂ Schottky diode. Response time of 15 s and response time of 1 s are obtained for the Schottky diode devices as the devices are exposed to 70-ppb NO₂ and 70-ppb NH₃ with a relative resistance change of 13% and 101% respectively at room temperature. Moreover, density function theory is used to support these results. Recently, it was reported that channel thickness had effects on gas-sensing application of MoTe₂ FETs (Figure 8c). MoTe₂ channel thickness ranges from 10.6 nm

to 56.7 nm and the conductivity type of the MoTe₂ FETs changes from p-type to ambipolar to n-type conduction. The modulation of the Schottky barrier height and related bandgap alignment account for the conducting behavior of MoTe₂ FETs varying. The above-mentioned phenomenon is also investigated in MoTe₂ FETs for NH₃ sensing, which confirms the p- and n-type behavior of MoTe₂ devices.¹¹⁵

It is noteworthy that sensors of 2D TMDs have commonly been shown to be less sensitive to NH₃ than NO₂, due to lower adsorption energy of channel materials for NH₃ molecules. SnS₂, as distinguished from MoS₂, has larger electronegativity, potentially enhancing gas adsorption ability. Chen et al.¹¹⁶ demonstrated suspended devices fabricated with SnS₂ exhibiting a higher sensitivity, faster response and recovery rates than traditional SnS₂ sensors upon light excitation (Figure 8d). At room temperature, the devices can detect NH₃ vapor even if the concentration is as low as 20 ppb and display high selectivity to NH₃ over many other chemical gases. There are two reasons for the enhancement of device performance. The designed suspended structure increases reaction area and the light excitation induces an increase of charge density. Suspended structure with light assistance is a method that can be applied to the other 2D TMD-based sensors. SnSe₂ is an anisotropic binary-layered material with rich physical properties, whose gas-sensing properties are investigated using first-principles calculations, and gas sensor mode is fabricated using few-layer SnSe₂ prepared by CVD method.¹¹⁷ Theoretical simulations demonstrate that electrons transfer direction is from SnSe₂ to NO₂. However, that is the opposite for NH₃. Notably, NO₂ adsorption will result in a flat molecular band around the Fermi energy and the induced molecular band is close to the minimum of conduction band. Moreover, there is lower adsorption energy for SnSe₂ adsorbing NO₂ than NH₃, NO₂ molecules adsorbed on SnSe₂ have a higher charge transfer value. A GaSe-based with strong selectivity and long-term stability is fabricated to detect NO₂.¹¹⁸ The sensitivity of this sensor is 0.5 ppb at room temperature, and the NO₂ selectivity ratio is 100 times than that of other interfering environmental gases. In practical terms the GaSe-based sensors can detect the vehicle exhaust emission and act as wearable NO₂ sensors. Usually, the performance of TMDs-based gas sensors is subject to sluggish and incomplete recovery at room temperature and the sensitivity is depressed by absorbed O₂. Ultrahigh and reversible responses are achieved using the InSe-based sensors by UV illumination for NO₂ detection.¹¹⁹

The limit of detection is 0.98 ppb, that is ~ 40 times lower than that without UV light. View Article Online
DOI: 10.1039/D2TA00075J

Inherent dangling bonds are absent on the surface of 2D TMDs, thus weaker Fermi level pinning effect emerges at the van der Waals interfaces of graphene/2D TMDs compared with original interfaces of graphene and bulk semiconductor. Tabata et al.¹²⁰ investigated gas-sensing characteristics of graphene/MoS₂ heterojunction resulted from gas induced modulation of Schottky barrier in the device (Figure 8e). Graphene/MoS₂ devices are passivated with gas barrier layers as only the gas-sensitive parts of graphene/MoS₂ heterojunction leave. The graphene/MoS₂ device exhibits a remarkable increase in resistance with a factor greater than 10³, upon exposure to 1 ppm NO₂ under reverse biases, which is revealed to be a direct reflection of the NO₂-induced increase in the Schottky barrier height. Moreover, the response shows strong dependence on the bias and back-gate voltages. A MSM diode model is used to illustrate these behaviors. Similarly, Pham et al.¹²¹ investigated the electrical properties in detail and application for detection of volatile organic compounds of devices with Schottky junction of MoS₂/graphene. Graphene, MoS₂ or MoS₂/graphene is used as the channel materials and 300 nm Si is utilized as the back gate in the FET devices. The observed in-built Schottky barrier height of the MoS₂/graphene heterostructure is 127 meV. Compared to graphene FETs, MoS₂/graphene FETs display a shift in potential at charge neutrality point (V_{CNP}) to lower gate voltage confirmed by photoluminescence (PL) quenching of MoS₂. The heterogeneity induced charge transfer in the heterostructure of MoS₂/graphene results in outstanding performance in chemical sensing. For the detection of toluene, the MoS₂/graphene FET-based sensor shows higher sensitivity and superior signal-to-noise ratio compared to MoS₂ or graphene individually.

Gas sensing, one of the considerable research fields of next generation smart e-skin, is beneficial to detect unhealthy gases in wearable electronics, to monitor human respiration or to examine specific disease-related gas molecules for diagnosis and therapy of diseases.¹²² The emerging atomically thin TMDs could be good candidates for e-skin sensors. Because they prove to be much lower intrinsic background carrier densities (less power consumption) unlike zero-bandgap graphene and great advance in scalable material synthesis will highly facilitate their device integration.¹²³ Herein, a large-area WS₂ film is synthesized by sulfurization of a tungsten film to fabricate humidity sensor. The sensor shows fine capability of humidity

sensing no matter the film is flat or is bent down to 5 mm.¹²⁴ Fast response as well as recovery times in a few seconds and conductivity dependent on relative humidity range (up to 90%) are observed for the WS₂ film. Then, a transparent, flexible, and stretchable humidity sensor is fabricated by using graphene as electrodes and thin polydimethylsiloxane (PDMS) as substrate (Figure 8f). This sensor can be attached to skin easily and operated as a moisture sensor under stretched, relaxed, and compressed states. The results illustrate these sensors enable real-time monitoring of human breath.

3.3. Schottky-contacted strain sensors

Single-atomic-layer MoS₂, MoSe₂ and WTe₂ have proved to show piezoelectricity derives from strain-induced lattice distortion and the associated ion charge polarization, which indicates rational exploitation of their remarkable semiconducting and mechanical properties to fabricate nanoscale electromechanical devices. Wu et al.¹²⁵ conducted an experiment to observe piezoelectricity in monolayer MoS₂ for the first time and demonstrated the application of mechanical energy harvesting and piezotronic sensing (Figure 9a). Oscillating electrical outputs are obtained by cyclic stretching and releasing of odd-layer MoS₂ flakes, producing transformation of mechanical energy into electricity. A monolayer flake outputs 15 mV and 20 pA as strained by 0.53%, corresponding to a power density of 2 mW/m² and a 5.08% mechanical-to-electrical energy conversion efficiency. Charge carrier transport at the MoS₂–metal barrier is modulated by strain-induced polarization charges resulting in enhanced strain sensing. Metal–MoS₂ contact is influenced by piezoelectric polarization charges at the zigzag edges directly. Because both concentration or distribution of free carriers in MoS₂ and electronic charges in interface states are affected,¹²⁶ and then the mechanical strain can act as a regulating gate signal. The research, strain-induced bandgap modulation and change of electrical properties on monolayer and few-layer MoS₂ in that case, is further conducted. Manzeli et al.¹²⁷ incorporated monolayer, bilayer, and trilayer MoS₂ in a nanoelectromechanical membrane configuration (Figure 9b). Measurements of electrical conductivity using an atomic force microscope indicate strain-induced band gap tuning and appearance of the piezoresistive effect in MoS₂. Finite element method (FEM) simulations are used to quantify the band gap change and to obtain a comprehensive picture of the spatially varying bandgap profile on the membrane. The piezoresistive gauge factors calculated by finite

element method are -148 ± 19 , -224 ± 19 , and -43.5 ± 11 for monolayer, bilayer, and trilayer MoS₂, respectively, which is 2 orders of magnitude higher than that of strain sensors with suspended graphene. It is important for a kind of NEMS (nanoelectromechanical systems) transducer to adjust the resistivity of 2D TMDs due to strain-induced bandgap regulation.

In addition, the strain sensitivity can be significantly tuned by adjusting the MoS₂ Fermi level by applying a gate bias. Tsai et al.¹²⁸ fabricated a piezoresistive strain sensor consisting of a flexible MoS₂ field-effect transistor based on uniform large-area trilayer films (Figure 9c). The strain sensitivity rises exceeding 1 order of magnitude due to modulation of MoS₂ Fermi level with gate bias. Band gap change deriving from strain will also account for piezoresistive effect in MoS₂, according to the results from optical spectroscopy. The gate-tunable gauge factor can be as high as -40 . For practical applications for sensing, transistor-based devices benefit from the gate-tunable piezoresistivity because alteration of gate bias changes the relative sensitivity to strain.

Strain-induced polarization charges will only accumulate at zigzag edges of CVD-grown monolayer MoS₂ under isotropic mechanical deformation, which has been rigorously investigated in some experiments. An experimental study of the piezoelectric effect in monolayer MoS₂ triangles prepared by CVD with isotropic distortion is conducted.¹²⁹ Strain/force sensors are also presented by using a monolayer MoS₂ with high sensitivity (Figure 9d).

Recently, the gauge factors of TMDs-based strain sensors have been greatly enhanced. The highest gauge factor for the strain sensor is about 1160, which is much larger than that of many conventional strain sensors.¹³⁰ Schottky barrier variation in strain sensors based on TMD/metal junctions is limited by almost constant work function of metal electrodes. Consequently, Lee et al.¹³⁰ fabricated a highly sensitive strain sensor based on adjustable Schottky barrier in a FET comprised of MoS₂/graphene heterostructure (Figure 9e). The Fermi level of graphene can be modulated largely for the low density of states near the Dirac point and corresponding Schottky barrier in a MoS₂/graphene junction can be adjusted by strain-induced polarized

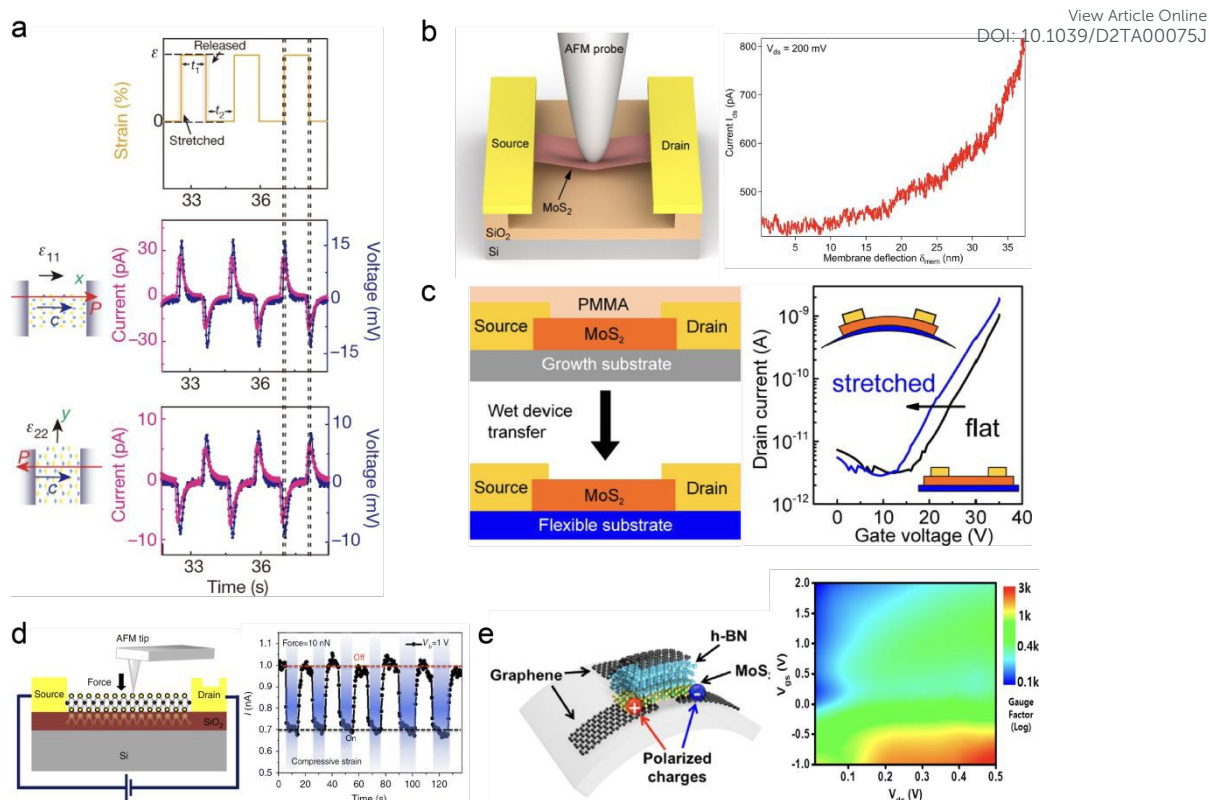


Figure 9. (a) Voltage response with 1GV external load and short-circuit current response. Top: applied strain as a function of time. Middle: corresponding piezoelectric outputs from single-atomic-layer MoS₂ when strain is applied in the x direction (armchair direction). Bottom: corresponding piezoelectric outputs from the same device when strain is applied in the y direction (zigzag direction). Reproduced with permission from ref. 125. Copyright 2014 Springer Nature. (b) Schematic drawing of the setup for direct current electrical characterization of suspended channel MoS₂ devices under strain and drain current as a function of membrane deflection at the center $\delta_{mem} = (z_{piezo} - \delta_{probe})$. Reproduced with permission from ref. 127. Copyright 2015 American Chemical Society. (c) Flexible MoS₂ field-effect transistors fabricated by using a device transfer technique and representative transfer curve (I_d - V_{bg}) of a flexible MoS₂ transistor measured in the flat state (black line) and the stretched state (blue line, applied strain $\epsilon = 0.07\%$). Reproduced with permission from ref. 128. Copyright 2015 American Chemical Society. (d) Schematic illustration of a MoS₂ device under mechanical load applied by an AFM tip and current response of CVD monolayer MoS₂ device at repeated compressive strains at a fixed bias voltage of 1V. Reproduced with permission from ref. 129. Copyright 2014 Springer Nature. (e) Schematic of the fabrication process of a flexible and transparent graphene/MoS₂ vdWH FET and Color map of gauge factor of a graphene/MoS₂ vdWH FET depending on V_{gs} and V_{ds} . Reproduced with permission from ref. 130. Copyright 2019 American Chemical Society.

charges of MoS₂. Theoretical simulations and temperature-dependent electrical measurements indicate that the Schottky barrier change ($\Delta\Phi_{SB}$) reaches a plateau when Fermi level of graphene is placed at the charge neutral (Dirac) point by changing gate voltage. The results show that the peak $\Delta\Phi_{SB}$ of 118 meV and corresponding ratio of current change of 978 are obtained under 0.17% strain, acquiring a great gauge factor of 575294.

As the sensitivity of TMDs-based strain sensors improves, TMDs can be used in the sensors to measure the ultrasmall mass accurately. Jiang et al.¹³¹ took advantage of resonant single-layer MoS₂ and its piezoelectrical effect to detect mass. The reported methods contain several strengths such as the driving forces coming from an alternating electric field, improvement of the measurement accuracies for the increase of piezo-operations, and fast measurements of GHz ranges. Finally, membrane motions at high vibrating speeds. The authors using the mass sensor to realize ~2406.26 MHz resonance for the piezoresonator when background noise is ~26.1 Hz in 300 K. Moreover, the resonant frequency shift of this MoS₂ resonator is used to detect biomolecules mass with much high resolution up to ~3.0 zg.

3.4. Schottky-contacted biosensors

TMDs may serve as promising materials for SERS for high specific surface area, isolation of highly active noble metal NPs from air, and substantial SERS “hot spots”.¹³² A SERS-active substrate with MoS₂@Ag (**Figure 10a**) is demonstrated to detect pesticide residues.¹³² Ag layer on the flower-like MoS₂ results in remarkable SERS effect and photocatalytic activity for generation of enough electromagnetic “hot spots”, and Schottky barrier between the Ag NPs and MoS₂ inhibits combination of electron–hole pairs. LOD (Limits of detection) of 6.4×10^{-7} and 9.8×10^{-7} mg/mL are obtained for the standard solutions of thiram (tetramethylthiuram disulfide, TMTD) and methyl parathion (MP) respectively using the recyclable MoS₂@Ag hybrid substrate and the hybrid substrate is used to detect TMTD and MP on eggplant, Chinese cabbage, grape, and strawberry. Utilization of MoS₂@Ag substrate enables to detect little mixtures of the residues on these fruits and vegetables simultaneously.

TMDs, kinds of excellent photoactive materials, are also beneficial to photoelectrochemical process. Ding et al. fabricated a photoelectric aptamer sensor to detect PRO (profenofos) by forming a suitable Schottky barrier between MoTe₂ nanoparticles (MoTe₂ NPs)/RGO (**Figure 10b**).¹³³ The Schottky barrier hinders the photogenic electrons

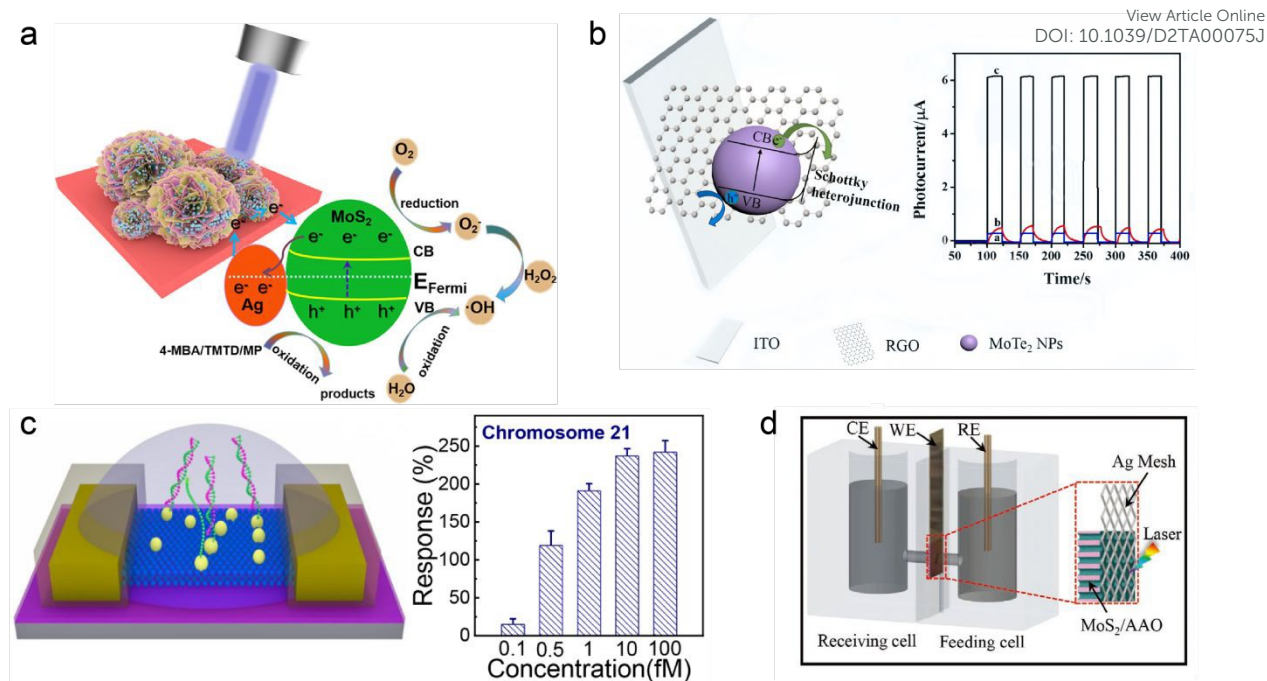


Figure 10. (a) Application of the flower-like MoS₂@Ag hybrid matrix in recyclable monitoring of pesticide residues. Reproduced with permission from ref. 132. Copyright 2020 American Chemical Society. (b) Photoelectric enhancement mechanism diagram and photocurrent of RGO, MoTe₂ NPs and MoTe₂ NPs/RGO. Reproduced with permission from ref. 133. Copyright 2020 Elsevier (c) The structure diagram and the response-concentration relation at V_{gs} = 0.8 V. Reproduced with permission from ref. 135. Copyright 2019 American Chemical Society. (d) Schematic illustration of a PEC biosensor based on MoS₂/AAO photoresponsive nanochannel. Reproduced with permission from ref. 136. Copyright 2020 Wiley.

returning to MoTe₂ and thus enhanced photoelectric properties can be observed. Photocurrent intensity of MoTe₂/RGO is much larger than both MoTe₂ NPs and RGO.

Atomic-scale thickness of 2D TMDs makes them the good candidates for nucleic acid detection. Apart from the expensive method such as PCR, WGS, biosensors based TMDs may be available to fast detect multiple disease markers with ultrahigh sensitivity. Farimani et al. applied atomistic and quantum simulations and suggested that a single-layer MoS₂ was an extraordinary material (with a SNR > 15) for DNA sequencing by two competing technologies (i.e., nanopore and nanochannel).¹³⁴ A MoS₂ nanopore shows four distinct ionic current signals for single-nucleobase detection with low noise. FET biosensors based on TMDs present the advantages of low cost, high speed, small size, and excellent compatibility with integrated circuits. The extremely sensitive FET sensors are constructed by using monolayer MoS₂ films to detection of DNA.¹³⁵ Specifically, MoS₂ functionalized with gold nanoparticles (Au NPs) can be immobilized with probe DNAs for the specific capture of target DNAs. The sensors are

used in noninvasive prenatal testing (NIPT) for trisomy 21 syndrome (Figure 10c). Detection limit below 100 aM is extracted for the FET biosensors as they detect target DNA fragments (chromosome 21 or 13). Moreover, high response reaches 240% with a high specificity, which suggests the potential for the screening Down syndrome. Importantly, the biosensor is able to monitor target DNA at concentrations as low as 1 fM in a real-time test. Artificial photoresponsive nanochannels have the capacity to achieve ion transport through light modulation, so they can be used for ultrasensitive nucleic acid detection. Au and MoS₂ modified porous anodic aluminum oxide (AAO) is utilized to detect miRNA-155 with high-performance (Figure 10d). AuNPs modified MoS₂/AAO displays much stronger current due to forming Au/MoS₂ Schottky junction that contributes to separation of electron-hole pairs.¹³⁶

4. Strategies for performance improvement of Schottky-contacted sensors

Here, we summarize the strategies for improving the performance of Schottky-contacted sensors. They include preparation methods, defect engineering, modulation of Schottky barrier, functional surface, and piezoelectric effect (Figure 11).

4.1. Preparation Methods

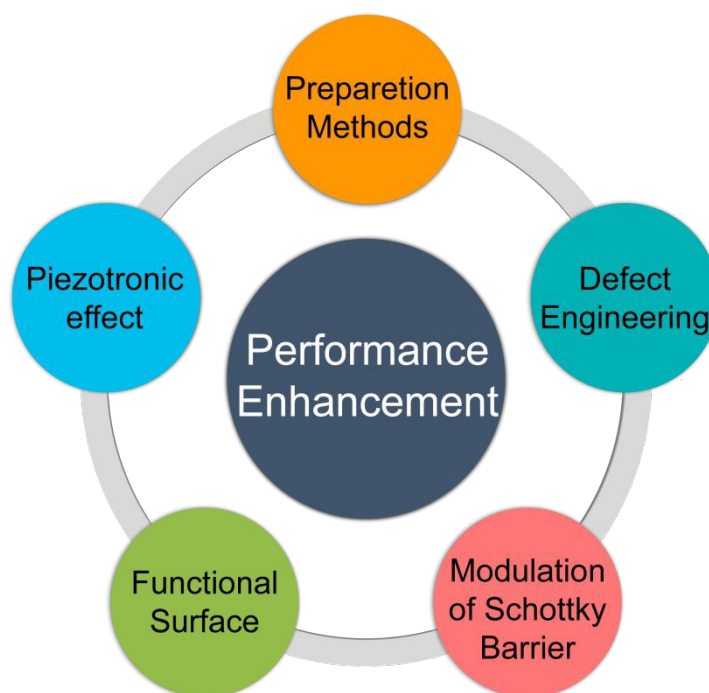


Figure 11. Performance improvement by different approaches for 2D TMDs-based Schottky-contacted sensors.

Different synthetic methods will remarkably influence the structure of as-obtained 2D TMDs, and thus, their properties and applications. In the initial part of the review, we have introduced some important methods to prepare 2D TMDs including exfoliation routes, vapor deposition and solution-based synthesis. When it comes to the selection of preparation methods, there are four critical criteria for making a decision covering lateral size, thickness, production rate and crystalline qualities. For example, the highest quality nanosheets can be obtained by mechanical cleavage; however, production rate of this method is rather low and long time is needed to search the samples carefully under a light microscope. The produced nanosheets by mechanical cleavage are randomly distributed on the substrate and there is no correlation between their lateral sizes and thicknesses. So, 2D TMDs obtained by this method are suitable for transistors, fundamental research and flexible electronics. Obviously, it makes a difference to modify the existing method to obtain better 2D TMDs. For example, in the solution-based method, when Li^+ is replaced by THAB (tetraheptylammonium bromide), the electrical performance and phase purity of the obtained MoS_2 are enhanced greatly. A field-effect transistor made from a single THAB-exfoliated nanosheet displays an electron mobility of about $10 \text{ cm}^2 \text{ V}^{-1} \text{ s}^{-1}$ and current modulation over five orders of magnitude which is much larger than that of Li-exfoliated MoS_2 .⁵⁷

4.2. Defect Engineering

Defect engineering provides a logical route to tune the properties of TMDC-based electronic devices through the healing of structural defects, changing the doping concentration or carrier types, and reducing contact resistance.⁴⁰

Optoelectronic performance of 2D TMDs is subject to intrinsic defects and extrinsic disorder. Engineering the chalcogen atom in the outmost layer can provide flexibility and versatility for modulating/improving their optoelectronic performance, such as detection range, energy gain, photoresponsivity, and photoconductance type.³⁹ Laser-induced local phase transitions in MoTe_2 can form an ohmic heterophase homojunction between semiconducting hexagonal (2H) and metallic monoclinic (1T') MoTe_2 , which increases the carrier mobility of the MoTe_2 transistor by a factor of about 50, while retaining a high on/off current ratio of 10^6 .¹³⁷ Defects, most likely sulfur divacancy with oxygen adsorption, may contribute to energy gained by

absorbing multiphonons through intermediate states, leading to anomalous energy upconversion. Wang et al. demonstrated a monolayer WS₂ photodetector that can detect photons with energy even lying 219 meV below the bandgap of WS₂ at room temperature. photoresponsivity ranges from 551 to 59 mA/W, as excitation wavelengths change from 620 to 680 nm. This anomalous phenomenon can be ascribed to energy upconversion.¹³⁸

Pristine TMDs weakly combine with nitrogen-containing gases (NCGs), so, it needs some improvement for the materials to be efficient sensing materials. Proper elemental substitutions facilitate the binding effect considerably. Panigrahi et al.¹³⁹ considered Ge (Sb) to substitute Se (Te) in MoSe₂ (MoTe₂) for tuning up the gas-sensing properties of these TMDs. In consequence, the NCGs molecules can adsorb on the substituted sheets with much higher binding energies. Both MoSe₂-Ge and MoTe₂-Sb are suitable materials for sensing applications. Gas sensors that work at elevated temperature in an inert atmosphere is not beneficial for practical application. However, a gas sensor based on oxygen-doped MoSe₂ hierarchical nanostructures can operate typically at 200 °C in air for fast and facile gas sensing of trimethylamine (TMA) effectively.¹⁴⁰ The mechanism of improving the performance of gas-sensing through oxygen doping has been investigated. The results suggest that the oxygen doping could greatly optimize the electronic structure, and thus regulate the Fermi level of MoSe₂ as well as the affinity between TMA molecules and sensor surface.

Sometimes, defects are not favorable, because they will weaken electrical properties and device performance of 2D TMDs. Therefore, restoring chalcogen atomic defects can promote the development of the properties and device performances of 2D TMDs significantly, while avoiding adverse effects. Zhang et al.¹⁴¹ proposed a powerful poly(4-styrenesulfonate) (PSS)-treated strategy to repair sulfur vacancy in monolayer MoS₂. The self-healing mechanism reveals that PSS-induced hydrogenation process promotes sulfur adatom clusters to heal the sulfur vacancies on the MoS₂ surface. The electron concentration of the self-healed MoS₂ dramatically decreases by 643 times, leading to a work function enhancement of ~150 meV.

4.3. Modulation of Schottky Barrier

It is of great flexibility to build and engineer 2D Schottky junctions exploiting the atomically flat, inert surface and van der Waals coupling of 2D materials. The behavior of Schottky

junction is determined by the Schottky barrier to manage electron/hole transport. Hence, modulation of the Schottky barrier height is a requisite for the engineering of sensors based on Schottky junction.

According to the Schottky–Mott relationship, it is simple to tailor the Schottky barrier by varying metals with different work functions or by regulating carrier doping in a semiconductor. However, Fermi level (FL) pinning makes the Schottky–Mott relation inaccurate by interface states in practice, and thus the Schottky-Mott rule is usually amended by a factor $S = |d\Phi_{SB}/d\Phi_M|$, which denotes the dependence of the Schottky barrier height on the metal's work function. Liu et al.¹⁴² demonstrated the Schottky barrier height, which approached the Schottky-Mott limit, was governed by the work function of the metal and was thus highly tunable. The detailed strategy is proposed by laminating atomically flat metal films onto two-dimensional semiconductors to create van der Waals metal-semiconductor junctions forming an interface where chemical disorder and Fermi-level pinning are not existing. The nondestructive method to integrate metal is suitable for fabricating high-performance electronics and optoelectronics.

Gating is efficient and helpful to adjust the performance of Schottky sensors by employing a positive or negative gate voltage at room temperature. Baek et al.¹⁴³ demonstrated a gas sensor based on MoSe₂ FETs with a maximum sensitivity of ~1907 for NO₂ gas concentration in the 100-300 ppm range. Compared with diode-like MoSe₂ sensors, the FET-based sensors exhibit great enhance of sensitivity for applying negative gate voltage. Triboelectric nanogenerators and similar tools are also suitable for modulation of Schottky barrier.^{144,145}

Interface modulation of the Schottky junction is also an approach to achieve selective and highly sensitive sensors. Yang et al.¹⁴⁶ took advantage of TiO₂ as the interfacial layer for Si/RGO Schottky sensor arrays, and thus sensitivity for 9 ppb 2,4,6-trinitrotoluene, 4.9 ppt hexogen and 0.25 ppq octogen was enhanced by 2.4, 7.5 and 5 times respectively.

4.4. Functional Surface

LSPR (localized surface plasmon resonance) of noble metal nanostructures always makes them display excellent light trapping and electromagnetic field enhancement properties, and can remarkably enhance the light-matter interaction around the nanostructures. Our group has

demonstrated the significant enhancement by LSPR for photodetection based on nanowires.^{147,148} LSPR enhanced the nanowire sensors. This strategy has great potential to achieve the enhancement of device performance.^{147,148} Coupling noble metal in nanoscale and 2D TMDs can enhance the performance of the sensors significantly. Sun et al.¹⁴⁹ demonstrated that a photodetector modified by Ag nanocubes exhibited prominent performance at low operating potential. External photoresponsivity of 7940 A/W is 38 times that of pristine MoS₂ photodetector as applying incident illumination of 2.2 pW. Ko et al.¹⁵⁰ also proved that surface functionalization by Ag nanowires (NWs) was useful to improve the gas-sensing performance of large-area WS₂ nanosheets. Large-area WS₂ nanosheets are synthesized through atomic layer deposition and then are sulfurized. The gas sensors fabricated by pristine WS₂ show strong response to acetone and NO₂ but incomplete recovery for sensing NO₂. After Ag NWs functionalization, the response (667%) and recovery of WS₂ gas sensor are highly enhanced upon exposure to NO₂. Surface functionalization is a powerful tool to achieve an excellent biosensor with high specificity. Jiao et al.¹³⁶ prepared a MoS₂/AAO nanochannel and the AuNPs immobilized by SH-modified probe RNA. Weak van der Waals makes the Au NPs assemble on MoS₂ flakes. The sensor detects miRNA-155 with ultrasensitive detection limit of 3 aM and barely responses to many other miRNAs.

4.5. Piezotronic effect

Piezotronic effect provides a powerful route to modify the electrical and optical properties of electronic materials.^{151,152} Piezotronic effect is using the piezoelectric polarization charges as a 'gate' to control the transport in semiconductors, especially in the Schottky junction or p-n junction.¹⁵³ Zhao et al.¹⁵⁴ demonstrated regulation of optical and electrical performance of a MoS₂ FET by piezoelectric in both static and dynamic manners. Capacitive coupling between the piezoelectret and MoS₂ FETs lets residual piezopotential modulate the Fermi level of MoS₂ effectively, beneficial to subsequent fabrication of sophisticated devices for programming the initial electrical property. Enhanced piezopotential for the external strain can further affect the energy band bend of MoS₂ channel, promoting stronger performance of strain sensors (large gauge factor ~4800, fast response time ~0.15 s, and good durability >1000 s). Gant et al.¹⁵⁵ studied flexible and transparent photodetectors based on single-layer MoS₂ under the

application of biaxial strain. It can tune the photoresponsivity (by 2–3 orders of magnitude), the response time (from <80 ms to 1.5 s), and the spectral bandwidth (with a gauge factor of 135 meV/% or 58 nm/%) of the device to control the level of strain.

5. Conclusions and perspectives

In summary, we have provided an extensive review of the construction of various Schottky-contacted sensors based on 2D TMDs. As a new class of materials, 2D materials have achieved great progress in preparation methods and the Schottky-contacted sensors fabricated from the materials operated well in many fields including photodetection, gas sensing, strain sensing, and biosensing.

We described recent advances in the development of the Schottky sensors based on the 2D TMDs to provide an overview of advances in controlling preparation, common device structures, and strategies for development of performance of the sensors. Various preparation methods to obtain specific material quality, accurate architecture, morphologies are discussed in detail here. We also discuss advances in the application of 2D TMDs for Schottky sensors in the context of four major groups of signal sources, including light, gases, strain, and biomolecules, from both an historical and analytical perspective.

Although Schottky sensors based on 2D TMDs have many advantages, such as high sensitivity, there are still some bottlenecks that need to be broken. Production method is the cornerstone of achieving real-world and significant applications, not only for 2D TMD nanomaterials, but also for many other 2D nanomaterials, such as graphene, phosphorene, *h*-BN, etc. To prepare high-quality large nanosheets, not only micromechanical cleavage is a lab-scale rapid route to be used in fundamental research, but chemical vapor deposition (CVD) should be the proper method. For producing small nanoparticles and nanosheets, the hydro/solvothermal ways and liquid phase exfoliation are given priority to other production methods, including intercalation and exfoliation that are applied independently or act as complementary methods. There are some inconsistencies in reported values, even for very common properties, such as the bandgap. Alloys, heterostructures and mixed phases of 2D TMDs are of great importance even in the future and the production methods suitable for them are worthy of studying. Flexible devices of TMDs will be very an important research field in

the near future. It is still difficult for direct growth of TMDs on flexible and transparent substrates for the certain preparation conditions. However, great effort has been paid to the low temperature growth of graphene, lack of studying growth TMDs at low temperature. There are two strategies for realizing better flexible devices of TMDs: 1) to find and synthesize some catalysts and 2) to search for polymer substrates that can bear high temperatures. The common methods to produce 2D TMDs are mostly studied for traditional TMDs such as MoS₂, WS₂, MoSe₂, et al. The methods should be expanded to emerging TMDs such as PtSe₂, NbSe₂ and TaS₂.

The multifunctional properties of 2D TMDs and Schottky-contacted excellent functions have already made the remarkable improvement in the selectivity, stability, and reproducibility of sensing devices to detect photo, gases, volatile organic compounds, strain and biomolecules. The gas sensors have excellent performance even can operate at room temperature, but more efforts are required to be devoted in addressing challenges such as low power operation in different interfering environments, speed, multifunctionality, and stability. Moreover, the gas sensors are mostly designed for NH₃ and NO₂ which limits their application widely, so, further investigations should major in some organic gases, moisture and other gas molecules. Flexibility of gas sensors based on Schottky contact is another considerable factor to meet the requirements of the wearable electronics. Flexibility of gas sensors can act as wearable electronic devices. Self-healing capability of the flexible sensors can be involved and further investigated. The flexibility of the devices can also be improved in the next study. Moreover, the lifetime of the flexible devices is also a key problem that should be paid attention to. The flexible devices for other sensors are also suitable for these investigation fields.

Photodetectors with Schottky contact configurations often display prominent performance such as fast response, high responsivity and quantum efficiencies exceeding 100% under external bias. However, there are still some obstacles to be overcome for Schottky-contacted photodetectors with 2D TMDs. Despite the strong light-matter interaction for 2D TMDs, some 2D TMDs have disadvantages of low carrier mobility, hindering device performance. It needs to explore the optimal size, shape, and thickness of the 2D TMDs for light absorption to enhance the performance of the photodetectors. Some new structures like quantum wells and superlattices are worth exploiting for advanced Schottky-contacted photodetectors of 2D

TMDs.

As high-performance piezoelectricity is found in monolayer TMDs, powerful strain sensors are highly desirable to be developed. Conductivity of TMD devices can be actively modulated by the piezoelectric polarization charge under strain variation. These polarization charges alter the Schottky barrier height on both contacts to achieve rather high sensitivity for strain sensors. However, mechanical–electronic devices based on TMDs may be developed through more investigations for current single function and architectures of the devices and little study on Schottky-contacted devices. In the future, the researches can focus on realizing more complicated devices, more excellent nanoelectromechanical systems, and further study of interaction between Schottky barrier and piezotronics. Strain sensors are suitable for flexible devices and can be fabricated as a sensor array that is compatible with applications for electronic skin (E-skin).

Schottky-contacted biosensors for 2D TMDs are relatively little and have some remarkable performance. Much efforts need to be devoted in developing kinds of biosensors in next research of this field, which is favorable for practical application and further mechanisms study. Stability of a biosensor is a persistent problem because of liquid condition during detection process. The encapsulation of micro-nano electrode is necessary. Performance optimization of Schottky-contacted biosensors for 2D TMDs is also the important focus to study. Because the ability to design such biosensors with targeted structure-property relationships remains an unresolved issue due to the limited understanding of growth mechanisms and possible host-guest interactions within the material. For the excellent mechanical properties such as robustness and flexibility of 2D TMDs, Schottky sensors based on them can be supported on flexible foils, for smart wearable technologies and for monitoring the human/environment interface. It is also an important study field.

2D TMDs-based self-powered sensors have been extensively studied as photodetectors. Although the research on self-powered photodetectors has made great progress, self-powered Schottky-contacted sensors in other fields are needed to meet higher end applications.

Acknowledgments

The authors are thankful for the support provided by the National Natural Science

Foundation of China (52002027, T2125003, 61875015), and the Natural Science Foundation of Beijing Municipality (2214083, JQ20038, L212010).

View Article Online

DOI: 10.1039/C2TA00075J

Conflict of Interest

The authors declare no conflict of interest.

References

- 1 Q. Shi, B. Dong, T. He, Z. Sun, J. Zhu, Z. Zhang and C. Lee, *InfoMat*, 2020, **2**, 1131-1162.
- 2 S. Ko, J. Na, Y. Moon, U. Zschieschang, R. Acharya, H. Klauk, G. Kim, M. Burghard and K. Kern, *ACS Appl. Mater. Interfaces*, 2017, **9**, 42912-42918.
- 3 W. Wu, L. Wang, R. Yu, Y. Liu, S. Wei, J. Hone and Z. L. Wang, *Adv. Mater.*, 2016, **28**, 8463-8468.
- 4 K. Zhang, M. Peng, A. Yu, Y. Fan, J. Zhai and Z. L. Wang, *Materials Horizons*, 2019, **6**, 826-833.
- 5 B. Cho, M. G. Hahm, M. Choi, J. Yoon, A. R. Kim, Y. J. Lee, S. G. Park, J. D. Kwon, C. S. Kim, M. Song, Y. Jeong, K. S. Nam, S. Lee, T. J. Yoo, C. G. Kang, B. H. Lee, H. C. Ko, P. M. Ajayan and D. H. Kim, *Sci. Rep.*, 2015, **5**, 8052.
- 6 B. Wang, H. Luo, X. Wang, E. Wang, Y. Sun, Y. Tsai, J. Dong, P. Liu, H. Li, Y. Xu, S. Tongay, K. Jiang, S. Fan and K. Liu, *Nano Res.*, 2020, **13**, 2035-2043.
- 7 D. Sarkar, W. Liu, X. Xie, A. C. Anselmo, S. Mitragotri and K. Banerjee, *ACS Nano*, 2014, **8**, 3992-4003.
- 8 L. Wang, Y. Wang, J. I. Wong, T. Palacios, J. Kong and H. Y. Yang, *Small*, 2014, **10**, 1101-1105.
- 9 M. Park, Y. J. Park, X. Chen, Y. Park, M. Kim and J. Ahn, *Adv. Mater.*, 2016, **28**, 2556-2562.
- 10 Y. J. Park, B. K. Sharma, S. M. Shinde, M. Kim, B. Jang, J. Kim and J. Ahn, *ACS Nano*, 2019, **13**, 3023-3030.
- 11 T. Liu, S. Liu, K. Tu, H. Schmidt, L. Chu, D. Xiang, J. Martin, G. Eda, C. A. Ross and S. Garaj, *Nat. Nanotechnol.*, 2019, **14**, 223-226.
- 12 J. Shim, S. W. Jang, J. Lim, H. Kim, D. Kang, K. Kim, S. Seo, K. Heo, C. Shin, H. Yu, S. Lee, D. Ko and J. Park, *Nanoscale*, 2019, **11**, 12871-12877.

- 13 X. Zhang, J. Grajal, J. L. Vazquez-Roy, U. Radhakrishna, X. Wang, W. Chern, L. Zhou, Y. Lin, P. Shen, X. Ji, X. Ling, A. Zubair, Y. Zhang, H. Wang, M. Dubey, J. Kong, M. Dresselhaus and T. Palacios, *Nature*, 2019, **566**, 368-372.
- 14 S. Chen, S. Huang, J. Hu, S. Fan, Y. Shang, M. E. Pam, X. Li, Y. Wang, T. Xu, Y. Shi and H. Y. Yang, *Nano-Micro Letters*, 2019, **11**, 80.
- 15 Y. Wang, G. Xing, Z. J. Han, Y. Shi, J. I. Wong, Z. X. Huang, K. K. Ostrikov and H. Y. Yang, *Nanoscale*, 2014, **6**, 8884-8890.
- 16 S. Yuan, S. Pang and J. Hao, *Applied Physics Reviews*, 2020, **7**, 21304.
- 17 J. Chen, G. Wang, Y. Tang, H. Tian, J. Xu, X. Dai, H. Xu, J. Jia, W. Ho and M. Xie, *ACS Nano*, 2017, **11**, 3282-3288.
- 18 J. Huang, H. Liu, B. Jin, M. Liu, Q. Zhang, L. Luo, S. Chu, S. Chu and R. Peng, *Nanotechnology*, 2017, **28**, 275704.
- 19 A. Castellanos-Gomez, R. Roldán, E. Cappelluti, M. Buscema, F. Guinea, H. S. J. van der Zant and G. A. Steele, *Nano Lett.*, 2013, **13**, 5361-5366.
- 20 X. Fang, C. Hua, C. Wu, X. Wang, L. Shen, Q. Kong, J. Wang, Y. Hu, Z. Wang and L. Chen, *Chemistry - A European Journal*, 2013, **19**, 5694-5700.
- 21 K. F. Mak, C. Lee, J. Hone, J. Shan and T. F. Heinz, *Phys. Rev. Lett.*, 2010, **105**, 136805.
- 22 W. Choi, N. Choudhary, G. H. Han, J. Park, D. Akinwande and Y. H. Lee, *Mater. Today*, 2017, **20**, 116-130.
- 23 J. Wei, Y. Li, L. Wang, W. Liao, B. Dong, C. Xu, C. Zhu, K. Ang, C. Qiu and C. Lee, *Nat. Commun.*, 2020, **11**.
- 24 S. Luo, K. Liao, P. Lei, T. Jiang, S. Chen, Q. Xie, W. Luo, W. Huang, S. Yuan, W. Jie and J. Hao, *Nanoscale*, 2021, **13**, 6654-6660.
- 25 C. Anichini, W. Czepa, D. Pakulski, A. Aliprandi, A. Ciesielski and P. Samori, *Chem. Soc. Rev.*, 2018, **47**, 4860-4908.
- 26 S. Manzeli, D. Ovchinnikov, D. Pasquier, O. V. Yazyev and A. Kis, *Nat. Rev. Mater.*, 2017, **2**, 17033.
- 27 A. Pulkin and O. V. Yazyev, *Phys. Rev. B*, 2016, **93**, 41419.
- 28 M. A. Helal, H. M. El-Sayed, A. A. Maarouf and M. M. Fadlallah, *Phys. Chem. Chem. Phys.*, 2021, **23**, 21183-21195.

- 29 M. Mathew and C. S. Rout, *J. Mater. Chem. C*, 2021, **9**, 395-416.
- 30 J. Meng and Z. Li, *Adv. Mater.*, 2020, **32**, 2000130.
- 31 M. Samadi, N. Sarikhani, M. Zirak, H. Zhang, H. Zhang and A. Z. Moshfegh, *Nanoscale Horizons*, 2017, **3**, 90-204.
- 32 A. Kumar and P. K. Ahluwalia, *Model. Simul. Mater. Sc.*, 2013, **21**, 065015.
- 33 F. A. Rasmussen and K. S. Thygesen, *The Journal of Physical Chemistry C*, 2015, **119**, 13169-13183.
- 34 H. Kim and H. J. Choi, *Phys. Rev. B*, 2021, **103**, 085404.
- 35 G. Mirabelli, C. McGeough, M. Schmidt, E. K. McCarthy, S. Monaghan, I. M. Povey, M. McCarthy, F. Gity, R. Nagle, G. Hughes, A. Cafolla, P. K. Hurley and R. Duffy, *J. Appl. Phys.*, 2016, **120**, 125102.
- 36 J. Pető, T. Ollár, P. Vancsó, Z. I. Popov, G. Z. Magda, G. Dobrik, C. Hwang, P. B. Sorokin and L. Tapasztó, *Nat. Chem.*, 2018, **10**, 1246-1251.
- 37 J. Gao, B. Li, J. Tan, P. Chow, T. Lu and N. Koratkar, *ACS Nano*, 2016, **10**, 2628-2635.
- 38 R. Yue, A. T. Barton, H. Zhu, A. Azcatl, L. F. Pena, J. Wang, X. Peng, N. Lu, L. Cheng, R. Addou, S. McDonnell, L. Colombo, J. W. P. Hsu, J. Kim, M. J. Kim, R. M. Wallace and C. L. Hinkle, *ACS Nano*, 2015, **9**, 474-480.
- 39 Q. Liang, Q. Zhang, X. Zhao, M. Liu and A. T. S. Wee, *ACS Nano*, 2021, **15**, 2165-2181.
- 40 Z. Hu, Z. Wu, C. Han, J. He, Z. Ni and W. Chen, *Chem. Soc. Rev.*, 2018, **47**, 3100-3128.
- 41 Q. H. Wang, K. Kalantar-Zadeh, A. Kis, J. N. Coleman and M. S. Strano, *Nat. Nanotechnol.*, 2012, **7**, 699-712.
- 42 B. W. H. Baugher, H. O. H. Churchill, Y. Yang and P. Jarillo-Herrero, *Nano Lett.*, 2013, **13**, 4212-4216.
- 43 H. Li, Z. Yin, Q. He, H. Li, X. Huang, G. Lu, D. W. H. Fam, A. I. Y. Tok, Q. Zhang and H. Zhang, *Small*, 2012, **8**, 63-67.
- 44 D. Tang, D. G. Kvashnin, S. Najmaei, Y. Bando, K. Kimoto, P. Koskinen, P. M. Ajayan, B. I. Yakobson, P. B. Sorokin, J. Lou and D. Golberg, *Nat. Commun.*, 2014, **5**, 3631.
- 45 Y. Huang, Y. Pan, R. Yang, L. Bao, L. Meng, H. Luo, Y. Cai, G. Liu, W. Zhao, Z. Zhou, L. Wu, Z. Zhu, M. Huang, L. Liu, L. Liu, P. Cheng, K. Wu, S. Tian, C. Gu, Y. Shi, Y. Guo, Z. G. Cheng, J. Hu, L. Zhao, G. Yang, E. Sutter, P. Sutter, Y. Wang, W. Ji, X. Zhou and H.

View Article Online
DOI: 10.1039/D2TA00075J

Gao, *Nat. Commun.*, 2020, **11**, 2453.

- 46 J. N. Coleman, M. Lotya, A. O'Neill, S. D. Bergin, P. J. King, U. Khan, K. Young, A. Gaucher, S. De, R. J. Smith, I. V. Shvets, S. K. Arora, G. Stanton, H. Kim, K. Lee, G. T. Kim, G. S. Duesberg, T. Hallam, J. J. Boland, J. J. Wang, J. F. Donegan, J. C. Grunlan, G. Moriarty, A. Shmeliov, R. J. Nicholls, J. M. Perkins, E. M. Grievson, K. Theuwissen, D. W. McComb, P. D. Nellist and V. Nicolosi, *Science*, 2011, **331**, 568-571.
- 47 M. Ayán-Varela, Ó. Pérez-Vidal, J. I. Paredes, J. M. Munuera, S. Villar-Rodil, M. Díaz-González, C. Fernández-Sánchez, V. S. Silva, M. Cicuéndez, M. Vila, A. Martínez-Alonso and J. M. D. Tascón, *ACS Appl. Mater. Interfaces*, 2017, **9**, 2835-2845.
- 48 G. Guan, S. Zhang, S. Liu, Y. Cai, M. Low, C. P. Teng, I. Y. Phang, Y. Cheng, K. L. Duei, B. M. Srinivasan, Y. Zheng, Y. Zhang and M. Han, *J. Am. Chem. Soc.*, 2015, **137**, 6152-6155.
- 49 Y. Ge, J. Wang, Z. Shi and J. Yin, *Journal of Materials Chemistry*, 2012, **22**, 17619.
- 50 C. Backes, B. M. Szydłowska, A. Harvey, S. Yuan, V. Vega-Mayoral, B. R. Davies, P. Zhao, D. Hanlon, E. J. G. Santos, M. I. Katsnelson, W. J. Blau, C. Gadermaier and J. N. Coleman, *ACS Nano*, 2015, **10**, 1589-1601.
- 51 K. R. Paton, E. Varrla, C. Backes, R. J. Smith, U. Khan, A. O'Neill, C. Boland, M. Lotya, O. M. Istrate, P. King, T. Higgins, S. Barwich, P. May, P. Puczkarski, I. Ahmed, M. Moebius, H. Pettersson, E. Long, J. Coelho, S. E. O'Brien, E. K. McGuire, B. M. Sanchez, G. S. Duesberg, N. McEvoy, T. J. Pennycook, C. Downing, A. Crossley, V. Nicolosi and J. N. Coleman, *Nat. Mater.*, 2014, **13**, 624-630.
- 52 E. Varrla, C. Backes, K. R. Paton, A. Harvey, Z. Gholamvand, J. McCauley and J. N. Coleman, *Chem. Mater.*, 2015, **27**, 1129-1139.
- 53 H. Yuan, X. Liu, L. Ma, P. Gong, Z. Yang, H. Wang, J. Wang and S. Yang, *RSC Adv.*, 2016, **6**, 82763-82773.
- 54 Z. Zeng, T. Sun, J. Zhu, X. Huang, Z. Yin, G. Lu, Z. Fan, Q. Yan, H. H. Hng and H. Zhang, *Angewandte Chemie*, 2012, **124**, 9186-9190.
- 55 Z. Zeng, Z. Yin, X. Huang, H. Li, Q. He, G. Lu, F. Boey and H. Zhang, *Angewandte Chemie International Edition*, 2011, **50**, 11093-11097.
- 56 A. Y. S. Eng, A. Ambrosi, Z. Sofer, P. Šimek and M. Pumera, *ACS Nano*, 2014, **8**, 12185-

12198.

View Article Online
DOI: 10.1039/D2TA00075J

- 57 Z. Lin, Y. Liu, U. Halim, M. Ding, Y. Liu, Y. Wang, C. Jia, P. Chen, X. Duan, C. Wang, F. Song, M. Li, C. Wan, Y. Huang and X. Duan, *Nature*, 2018, **562**, 254-258.
- 58 Z. Cai, B. Liu, X. Zou and H. Cheng, *Chem. Rev.*, 2018, **118**, 6091-6133.
- 59 Y. He, A. Sobhani, S. Lei, Z. Zhang, Y. Gong, Z. Jin, W. Zhou, Y. Yang, Y. Zhang, X. Wang, B. Yakobson, R. Vajtai, N. J. Halas, B. Li, E. Xie and P. Ajayan, *Adv. Mater.*, 2016, **28**, 5126-5132.
- 60 B. Liu, M. Fathi, L. Chen, A. Abbas, Y. Ma and C. Zhou, *ACS Nano*, 2015, **9**, 6119-6127.
- 61 Q. Ji, Y. Zhang, T. Gao, Y. Zhang, D. Ma, M. Liu, Y. Chen, X. Qiao, P. Tan, M. Kan, J. Feng, Q. Sun and Z. Liu, *Nano Lett.*, 2013, **13**, 3870-3877.
- 62 Y. Gong, B. Li, G. Ye, S. Yang, X. Zou, S. Lei, Z. Jin, E. Bianco, S. Vinod, B. I. Yakobson, J. Lou, R. Vajtai, W. Zhou and P. M. Ajayan, *2D Materials*, 2017, **4**, 21028.
- 63 Y. Zhang, Y. Zhang, Q. Ji, J. Ju, H. Yuan, J. Shi, T. Gao, D. Ma, M. Liu, Y. Chen, X. Song, H. Y. Hwang, Y. Cui and Z. Liu, *ACS Nano*, 2013, **7**, 8963-8971.
- 64 L. Chen, B. Liu, M. Ge, Y. Ma, A. N. Abbas and C. Zhou, *ACS Nano*, 2015, **9**, 8368-8375.
- 65 A. L. Elías, N. Perea-López, A. Castro-Beltrán, A. Berkdemir, R. Lv, S. Feng, A. D. Long, T. Hayashi, Y. A. Kim, M. Endo, H. R. Gutiérrez, N. R. Pradhan, L. Balicas, T. E. Mallouk, F. López-Urías, H. Terrones and M. Terrones, *ACS Nano*, 2013, **7**, 5235-5242.
- 66 Z. Tu, G. Li, X. Ni, L. Meng, S. Bai, X. Chen, J. Lou and Y. Qin, *Appl. Phys. Lett.*, 2016, **109**, 223101.
- 67 J. Zhang, H. Yu, W. Chen, X. Tian, D. Liu, M. Cheng, G. Xie, W. Yang, R. Yang, X. Bai, D. Shi and G. Zhang, *ACS Nano*, 2014, **8**, 6024-6030.
- 68 Y. Rong, Y. Fan, A. Leen Koh, A. W. Robertson, K. He, S. Wang, H. Tan, R. Sinclair and J. H. Warner, *Nanoscale*, 2014, **6**, 12096-12103.
- 69 J. Chen, B. Liu, Y. Liu, W. Tang, C. T. Nai, L. Li, J. Zheng, L. Gao, Y. Zheng, H. S. Shin, H. Y. Jeong and K. P. Loh, *Adv. Mater.*, 2015, **27**, 6722-6727.
- 70 J. Zhou, F. Liu, J. Lin, X. Huang, J. Xia, B. Zhang, Q. Zeng, H. Wang, C. Zhu, L. Niu, X. Wang, W. Fu, P. Yu, T. Chang, C. Hsu, D. Wu, H. Jeng, Y. Huang, H. Lin, Z. Shen, C. Yang, L. Lu, K. Suenaga, W. Zhou, S. T. Pantelides, G. Liu and Z. Liu, *Adv. Mater.*, 2017, **29**, 1603471.

- 71 Z. Yan, Z. Peng and J. M. Tour, *Accounts Chem. Res.*, 2014, **47**, 1327-1337.
- 72 D. Dumcenco, D. Ovchinnikov, K. Marinov, P. Lazic, M. Gibertini, N. Marzari, S. O. Lopez, Y. C. Kung, D. Krasnozhan, M. W. Chen, S. Bertolazzi, P. Gillet, I. M. A. Fontcuberta, A. Radenovic and A. Kis, *ACS Nano*, 2015, **9**, 4611-4620.
- 73 M. Xia, B. Li, K. Yin, G. Capellini, G. Niu, Y. Gong, W. Zhou, P. M. Ajayan and Y. Xie, *ACS Nano*, 2015, **9**, 12246-12254.
- 74 X. Liu, J. Wu, W. Yu, L. Chen, Z. Huang, H. Jiang, J. He, Q. Liu, Y. Lu, D. Zhu, W. Liu, P. Cao, S. Han, X. Xiong, W. Xu, J. Ao, K. Ang and Z. He, *Adv. Funct. Mater.*, 2017, **27**, 1606469.
- 75 Y. Zhan, Z. Liu, S. Najmaei, P. M. Ajayan and J. Lou, *Small*, 2012, **8**, 966-971.
- 76 J. Chen, X. Zhao, S. J. R. Tan, H. Xu, B. Wu, B. Liu, D. Fu, W. Fu, D. Geng, Y. Liu, W. Liu, W. Tang, L. Li, W. Zhou, T. C. Sum and K. P. Loh, *J. Am. Chem. Soc.*, 2017, **139**, 1073-1076.
- 77 Y. Gong, G. Ye, S. Lei, G. Shi, Y. He, J. Lin, X. Zhang, R. Vajtai, S. T. Pantelides, W. Zhou, B. Li and P. M. Ajayan, *Adv. Funct. Mater.*, 2016, **26**, 2009-2015.
- 78 S. M. Eichfeld, L. Hossain, Y. Lin, A. F. Piasecki, B. Kupp, A. G. Birdwell, R. A. Burke, N. Lu, X. Peng, J. Li, A. Azcatl, S. McDonnell, R. M. Wallace, M. J. Kim, T. S. Mayer, J. M. Redwing and J. A. Robinson, *ACS Nano*, 2015, **9**, 2080-2087.
- 79 K. Kang, S. Xie, L. Huang, Y. Han, P. Y. Huang, K. F. Mak, C. Kim, D. Muller and J. Park, *Nature*, 2015, **520**, 656-660.
- 80 Y. Gong, J. Lin, X. Wang, G. Shi, S. Lei, Z. Lin, X. Zou, G. Ye, R. Vajtai, B. I. Yakobson, H. Terrones, M. Terrones, B. K. Tay, J. Lou, S. T. Pantelides, Z. Liu, W. Zhou and P. M. Ajayan, *Nat. Mater.*, 2014, **13**, 1135-1142.
- 81 Y. Shi, W. Zhou, A. Lu, W. Fang, Y. Lee, A. L. Hsu, S. M. Kim, K. K. Kim, H. Y. Yang, L. Li, J. Idrobo and J. Kong, *Nano Lett.*, 2012, **12**, 2784-2791.
- 82 Y. Gong, S. Lei, G. Ye, B. Li, Y. He, K. Keyshar, X. Zhang, Q. Wang, J. Lou, Z. Liu, R. Vajtai, W. Zhou and P. M. Ajayan, *Nano Lett.*, 2015, **15**, 6135-6141.
- 83 S. Wang, X. Wang and J. H. Warner, *ACS Nano*, 2015, **9**, 5246-5254.
- 84 Y. Yoo, Z. P. Degregorio and J. E. Johns, *J. Am. Chem. Soc.*, 2015, **137**, 14281-14287.
- 85 T. W. Scharf, S. V. Prasad, T. M. Mayer, R. S. Goeke and M. T. Dugger, *J. Mater. Res.*,

2004, **19**, 3443-3446.

View Article Online
DOI: 10.1039/D2TA00075J

- 86 L. K. Tan, B. Liu, J. H. Teng, S. Guo, H. Y. Low and K. P. Loh, *Nanoscale*, 2014, **6**, 10584-10588.
- 87 T. Jurca, M. J. Moody, A. Henning, J. D. Emery, B. Wang, J. M. Tan, T. L. Lohr, L. J. Lauhon and T. J. Marks, *Angewandte Chemie*, 2017, **129**, 5073-5077.
- 88 H. D. Phan, Y. Kim, J. Lee, R. Liu, Y. Choi, J. H. Cho and C. Lee, *Adv. Mater.*, 2017, **29**, 1603928.
- 89 Y. Ho, C. Ma, T. Luong, L. Wei, T. Yen, W. Hsu, W. Chang, Y. Chu, Y. Tu, K. P. Pande and E. Y. Chang, *physica status solidi (RRL) – Rapid Research Letters*, 2015, **9**, 187-191.
- 90 C. R. Serrao, A. M. Diamond, S. Hsu, L. You, S. Gadgil, J. Clarkson, C. Carraro, R. Maboudian, C. Hu and S. Salahuddin, *Appl. Phys. Lett.*, 2015, **106**, 52101.
- 91 M. I. Serna, S. H. Yoo, S. Moreno, Y. Xi, J. P. Oviedo, H. Choi, H. N. Alshareef, M. J. Kim, M. Minary-Jolandan and M. A. Quevedo-Lopez, *ACS Nano*, 2016, **10**, 6054-6061.
- 92 L. El Bouanani, M. I. Serna, S. M. N. Hasan, B. L. Murillo, S. Nam, H. Choi, H. N. Alshareef and M. A. Quevedo-Lopez, *ACS Appl. Mater. Interfaces*, 2020, **12**, 51645-51653.
- 93 L. Cai, J. He, Q. Liu, T. Yao, L. Chen, W. Yan, F. Hu, Y. Jiang, Y. Zhao, T. Hu, Z. Sun and S. Wei, *J. Am. Chem. Soc.*, 2015, **137**, 2622-2627.
- 94 D. Son, S. I. Chae, M. Kim, M. K. Choi, J. Yang, K. Park, V. S. Kale, J. H. Koo, C. Choi, M. Lee, J. H. Kim, T. Hyeon and D. Kim, *Adv. Mater.*, 2016, **28**, 9326-9332.
- 95 A. Giri, H. Yang, K. Thiyagarajan, W. Jang, J. M. Myoung, R. Singh, A. Soon, K. Cho and U. Jeong, *Adv. Mater.*, 2017, **29**, 1700291.
- 96 K. C. Kwon, C. Kim, Q. V. Le, S. Gim, J. Jeon, J. Y. Ham, J. Lee, H. W. Jang and S. Y. Kim, *ACS Nano*, 2015, **9**, 4146-4155.
- 97 Y. R. Lim, W. Song, J. K. Han, Y. B. Lee, S. J. Kim, S. Myung, S. S. Lee, K. An, C. Choi and J. Lim, *Adv. Mater.*, 2016, **28**, 5025-5030.
- 98 W. Zhang, M. Chiu, C. Chen, W. Chen, L. Li and A. T. S. Wee, *ACS Nano*, 2014, **8**, 8653-8661.
- 99 X. Wang, H. Zhao, S. Shen, Y. Pang, P. Shao, Y. Li, N. Deng, Y. Li, Y. Yang and T. Ren, *Appl. Phys. Lett.*, 2016, **109**, 201904.
- 100 Y. Son, M. Li, C. Cheng, K. Wei, P. Liu, Q. H. Wang, L. Li and M. S. Strano, *Nano Lett.*,

2016, **16**, 3571-3577.

101 H. Wu, H. Si, Z. Zhang, Z. Kang, P. Wu, L. Zhou, S. Zhang, Z. Zhang, Q. Liao and Y. Zhang, *Advanced Science*, 2018, **5**, 1801219.

102 M. Luo, F. Wu, M. Long and X. Chen, *Nanotechnology*, 2018, **29**, 444001.

103 J. Wu, Y. T. Chun, S. Li, T. Zhang and D. Chu, *ACS Appl. Mater. Interfaces*, 2018, **10**, 24613-24619.

104 J. Liu, X. Liu, Z. Chen, L. Miao, X. Liu, B. Li, L. Tang, K. Chen, Y. Liu, J. Li, Z. Wei and X. Duan, *Nano Res.*, 2019, **12**, 463-468.

105 X. Sun, J. Sun, J. Xu, Z. Li, R. Li, Z. Yang, F. Ren, Y. Jia and F. Chen, *Small*, 2021, **17**, 2102351.

106 J. Chen, W. Ouyang, W. Yang, J. He and X. Fang, *Adv. Funct. Mater.*, 2020, **30**, 1909909.

107 C. Zhou, S. Raju, B. Li, M. Chan, Y. Chai and C. Y. Yang, *Adv. Funct. Mater.*, 2018, **28**, 1802954.

108 M. Dai, H. Chen, R. Feng, W. Feng, Y. Hu, H. Yang, G. Liu, X. Chen, J. Zhang, C. Xu and P. Hu, *ACS Nano*, 2018, **12**, 8739-8747.

109 H. Jang, Y. Seok, Y. Choi, S. H. Cho, K. Watanabe, T. Taniguchi and K. Lee, *Adv. Funct. Mater.*, 2021, **31**, 2006788.

110 F. Gong, H. Fang, P. Wang, M. Su, Q. Li, J. C. Ho, X. Chen, W. Lu, L. Liao, J. Wang and W. Hu, *Nanotechnology*, 2017, **28**, 484002.

111 M. Luo, F. Wu, M. Long and X. Chen, *Nanotechnology*, 2018, **29**, 444001.

112 H. Yang, S. Cai, D. Wu and X. Fang, *Advanced Electronic Materials*, 2020, **6**, 2000659.

113 B. Liu, L. Chen, G. Liu, A. N. Abbas, M. Fathi and C. Zhou, *ACS Nano*, 2014, **8**, 5304-5314.

114 I. Shackery, A. Pezeshki, J. Y. Park, U. Palanivel, H. J. Kwon, H. S. Yoon, S. Im, J. S. Cho and S. C. Jun, *J. Mater. Chem. C*, 2018, **6**, 10714-10722.

115 A. Rani, K. DiCamillo, M. A. H. Khan, M. Paranjape and M. E. Zaghoul, *Sensors-Basel*, 2019, **19**, 2551.

116 H. Chen, Y. Chen, H. Zhang, D. W. Zhang, P. Zhou and J. Huang, *Adv. Funct. Mater.*, 2018, **28**, 1801035.

117 Ó. L. Camargo Moreira, W. Cheng, H. Fuh, W. Chien, W. Yan, H. Fei, H. Xu, D. Zhang,

- Y. Chen, Y. Zhao, Y. Lv, G. Wu, C. Lv, S. K. Arora, C. Ó Coileáin, C. Heng, C. Chang and H. Wu, *ACS Sensors*, 2019, **4**, 2546-2552.
- 118 Y. F. Zhao, H. R. Fuh, C. Ó. Coileáin, C. P. Cullen, T. Stimpel Lindner, G. S. Duesberg, Ó. Leonardo Camargo Moreira, D. Zhang, J. Cho, M. Choi, B. S. Chun, C. R. Chang and H. C. Wu, *Advanced Materials Technologies*, 2020, **5**, 1901085.
- 119 L. Zhang, Z. Li, J. Liu, Z. Peng, J. Zhou, H. Zhang and Y. Li, *Anal. Chem.*, 2020, **92**, 11277-11287.
- 120 H. Tabata, Y. Sato, K. Oi, O. Kubo and M. Katayama, *ACS Appl. Mater. Interfaces*, 2018, **10**, 38387-38393.
- 121 T. Pham, P. Ramnani, C. C. Villarreal, J. Lopez, P. Das, I. Lee, M. R. Neupane, Y. Rheem and A. Mulchandani, *Carbon*, 2019, **142**, 504-512.
- 122 X. Wang, L. Dong, H. Zhang, R. Yu, C. Pan and Z. L. Wang, *Advanced Science*, 2015, **2**, 1500169.
- 123 Y. Shi, H. Li and L. J. Li, *Chem. Soc. Rev.*, 2015, **44**, 2744-2756.
- 124 H. Y. Guo, C. Y. Lan, Z. F. Zhou, P. H. Sun, D. P. Wei and C. Li, *Nanoscale*, 2017, **9**, 6246-6253.
- 125 W. Wu, L. Wang, Y. Li, F. Zhang, L. Lin, S. Niu, D. Chenet, X. Zhang, Y. Hao, T. F. Heinz, J. Hone and Z. L. Wang, *Nature*, 2014, **514**, 470-474.
- 126 Z. L. Wang, *Nano Today*, 2010, **5**, 540-552.
- 127 S. Manzeli, A. Allain, A. Ghadimi and A. Kis, *Nano Lett.*, 2015, **15**, 5330-5335.
- 128 M. Tsai, A. Tarasov, Z. R. Hesabi, H. Taghinejad, P. M. Campbell, C. A. Joiner, A. Adibi and E. M. Vogel, *ACS Appl. Mater. Interfaces*, 2015, **7**, 12850-12855.
- 129 J. Qi, Y. Lan, A. Z. Stieg, J. Chen, Y. Zhong, L. Li, C. Chen, Y. Zhang and K. L. Wang, *Nat. Commun.*, 2015, **6**, 7430.
- 130 I. Lee, W. T. Kang, Y. S. Shin, Y. R. Kim, U. Y. Won, K. Kim, D. L. Duong, K. Lee, J. Heo, Y. H. Lee and W. J. Yu, *ACS Nano*, 2019, **13**, 8392-8400.
- 131 C. Jiang, Q. Li, J. Huang, S. Bi, R. Ji and Q. Guo, *ACS Appl. Mater. Interfaces*, 2020, **12**, 41991-41998.
- 132 Y. Chen, H. Liu, Y. Tian, Y. Du, Y. Ma, S. Zeng, C. Gu, T. Jiang and J. Zhou, *ACS Appl. Mater. Interfaces*, 2020, **12**, 14386-14399.

- 133 L. Ding, J. Wei, Y. Qiu, Y. Wang, Z. Wen, J. Qian, N. Hao, C. Ding, Y. Li and K. Wang, *Chem. Eng. J.*, 2021, **407**, 127213.
- 134 A. B. Farimani, K. Min and N. R. Aluru, *ACS Nano*, 2014, **8**, 7914-7922.
- 135 J. Liu, X. Chen, Q. Wang, M. Xiao, D. Zhong, W. Sun, G. Zhang and Z. Zhang, *Nano Lett.*, 2019, **19**, 1437-1444.
- 136 S. Jiao, L. Liu, J. Wang, K. Ma and J. Lv, *Small*, 2020, **16**, 2001223.
- 137 S. Cho, S. Kim, J. H. Kim, J. Zhao, J. Seok, D. H. Keum, J. Baik, D. H. Choe, K. J. Chang, K. Suenaga, S. W. Kim, Y. H. Lee and H. Yang, *Science*, 2015, **349**, 625-628.
- 138 Q. Wang, Q. Zhang, X. Zhao, Y. J. Zheng, J. Wang, X. Luo, J. Dan, R. Zhu, Q. Liang, L. Zhang, P. K. J. Wong, X. He, Y. L. Huang, X. Wang, S. J. Pennycook, G. Eda and A. T. S. Wee, *Nano Lett.*, 2019, **19**, 5595-5603.
- 139 P. Panigrahi, T. Hussain, A. Karton and R. Ahuja, *ACS Sensors*, 2019, **4**, 2646-2653.
- 140 N. Hou, Q. Sun, J. Yang, S. You, Y. Cheng, Q. Xu, W. Li, S. Xing, L. Zhang, J. Zhu and Q. Yang, *Nano Res.*, 2020, **13**, 1704-1712.
- 141 X. Zhang, Q. Liao, S. Liu, Z. Kang, Z. Zhang, J. Du, F. Li, S. Zhang, J. Xiao, B. Liu, Y. Ou, X. Liu, L. Gu and Y. Zhang, *Nat. Commun.*, 2017, **8**, 15881.
- 142 Y. Liu, J. Guo, E. Zhu, L. Liao, S. Lee, M. Ding, I. Shakir, V. Gambin, Y. Huang and X. Duan, *Nature*, 2018, **557**, 696-700.
- 143 J. Baek, D. Yin, N. Liu, I. Omkaram, C. Jung, H. Im, S. Hong, S. M. Kim, Y. K. Hong, J. Hur, Y. Yoon and S. Kim, *Nano Res.*, 2017, **10**, 1861-1871.
- 144 J. Meng, H. Li, L. Zhao, J. Lu, C. Pan, Y. Zhang and Z. Li, *Nano Lett.*, 2020, **20**, 4968-4974.
- 145 J. Meng, Q. Li, J. Huang and Z. Li, *Nanoscale*, 2021, **13**, 17101-17105.
- 146 Z. Yang, X. Dou, S. Zhang, L. Guo, B. Zu, Z. Wu and H. Zeng, *Adv. Funct. Mater.*, 2015, **25**, 4039-4048.
- 147 Q. Li, J. Meng, J. Huang and Z. Li, *Adv. Funct. Mater.*, 2021, 2108903.
- 148 J. Meng, Q. Li, J. Huang, C. Pan and Z. Li, *Nano Today*, 2022, **43**, 101399.
- 149 B. Sun, Z. Wang, Z. Liu, X. Tan, X. Liu, T. Shi, J. Zhou and G. Liao, *Adv. Funct. Mater.*, 2019, **29**, 1900541.
- 150 K. Y. Ko, J. Song, Y. Kim, T. Choi, S. Shin, C. W. Lee, K. Lee, J. Koo, H. Lee, J. Kim,

T. Lee, J. Park and H. Kim, *ACS Nano*, 2016, **10**, 9287-9296.

View Article Online
DOI: 10.1039/D2TA00075J

151 Y. Yu and X. Wang, *Adv. Mater.*, 2018, **30**, 1800154.

152 F. Yang, J. Li, Y. Long, Z. Zhang, L. Wang, J. Sui, Y. Dong, Y. Wang, R. Taylor, D. Ni, W. Cai, P. Wang, T. Hacker and X. Wang, *Science*, 2021, **373**, 337-342.

153 Q. Li, J. Huang, J. Meng and Z. Li, *Adv. Opt. Mater.*, 2022, 2102468.

154 J. Zhao, Z. Wei, Q. Zhang, H. Yu, S. Wang, X. Yang, G. Gao, S. Qin, G. Zhang, Q. Sun and Z. L. Wang, *ACS Nano*, 2018, **13**, 582-590.

155 P. Gant, P. Huang, D. Pérez De Lara, D. Guo, R. Frisenda and A. Castellanos-Gomez, *Mater. Today*, 2019, **27**, 8-13.